CHALMERS
UNIVERSITY OF TECHNOLOGY

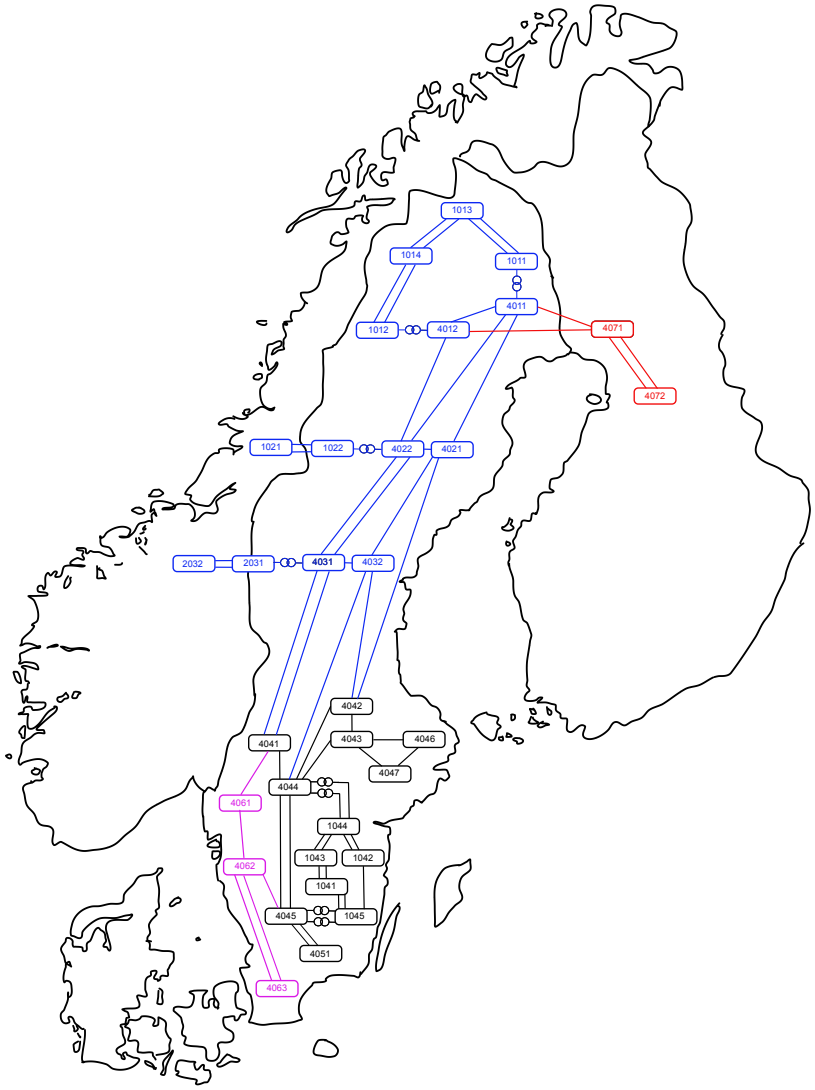

Ancillary Service for Frequency Support

Design of a Battery Storage Based Ancillary Service for Frequency Support in the Nordic Power System

Master's thesis in Electric Power Engineering

OMAR JUÁREZ MORENO

Department of Energy and Environment
CHALMERS UNIVERSITY OF TECHNOLOGY
Gothenburg, Sweden 2017

Master's thesis 2017

Ancillary Service for Frequency Support

Design of a Battery Storage Based Ancillary Service for Frequency Support in the Nordic Power System

OMAR JUÁREZ MORENO

CHALMERS
UNIVERSITY OF TECHNOLOGY

Department of Energy and Environment
Division of Electric Power Engineering
Chalmers University of Technology
Gothenburg, Sweden 2017

Ancillary Service for Frequency Support
Design of a Battery Storage Based Ancillary Service for Frequency Support in the Nordic Power System
OMAR JUÁREZ MORENO

Supervisor: Oscar Lennerhag, STRI AB
Examiner: Peiyuan Chen, Department of Energy and Environment

Master's Thesis 2017
Department of Energy and Environment
Division of Electric Power Engineering
Chalmers University of Technology
SE - 412 96 Gothenburg
Telephone +46 31 772 1000

Cover: Nordic32.

Typeset in LaTeX
Printed by Chalmers Reproservice
Gothenburg, Sweden 2017

Ancillary Service for Frequency Support
Design of a Battery Storage Based Ancillary Service for Frequency Support in the Nordic Power System
OMAR JUÁREZ MORENO
Department of Energy and Environment
Chalmers University of Technology

Abstract

In recent years, the frequency in the Nordic power system has been experiencing an increasing number of minutes outside the normal frequency band of ±100 mHz determined by ENTSO-E. It could be argued, that this trend is expected to continue, specially with the current tendency to replace conventional generation with intermittent, renewable energy sources that are decoupled from the grid. This in turn, has given rise to new opportunities in the Ancillary Service (AS) market, that can take advantage of network connected devices such as Energy Storage Systems (ESS), to increase the grid's flexibility.

This thesis deals with the design and implementation of a Battery Energy Storage System (BESS) that aims to provide the grid with frequency support in the frame of the Nordic reserve product Frequency Containment Reserve for Disturbance operation (FCR-D). The proposed Ancillary Service (AS) consists of a dynamic battery model that is controlled with an energy-curtailment strategy dependant on its State of Charge (SOC). The control system for the Voltage Source Converter (VSC) that interfaces the battery with the grid is conformed of a two-degree-of-freedom current controller implemented in the synchronous reference frame that receives the active and reactive power references from the outer frequency and voltage controllers, respectively.

The proposed AS was implemented using the simulation tool DIgSILENT PowerFactory. The models were tested in CIGRÉ's Nordic32A bus system with three different study cases: the loss of a generating unit that caused the frequency to drop below 49 Hz, where it was proven that a 50 MW, 300 MW h BESS could reduce the Nadir enough to avoid the activation of more drastic frequency-controlled actions. The second scenario explored the effect of converter rating versus battery capacity when the BESS is providing FCR-D, where it was concluded that the BESS capacity is not the limiting factor for providing the service but rather the converter's rating. Finally, the impact of the BESS was studied in a weaker grid where conventional generation was replaced with static generation. Here, it was shown that the proposed AS effect was more noticeable in the weaker grid, where the same BESS was able to reduce the Nadir by an additional 8.11% for the same frequency event, compared to the base case where no conventional generation was phased-out.

Keywords: Battery energy storage system, ancillary service, frequency control, Nordic power system, VSC control.

Acknowledgements

First and foremost, I would like to credit Chalmers University of Technology for awarding me the *Avancez* Scholarship that made it possible for me to study my master's degree in this prestigious university.

Secondly, I wish to acknowledge STRI AB for having sponsored this thesis, specially Pablo Rey, VD of Consulting Services.

Next, I would like to express my appreciation to Emil Hillberg, for granting me the opportunity to conduct my thesis at STRI Göteborg.

I would also like to convey my deep gratitude to my supervisor Oscar Lennerhag, for his patient guidance, enthusiastic encouragement and useful critiques of this master's thesis.

My grateful thanks are extended to my examiner Peiyuan Chen, for his useful and constructive recommendations on this project.

Advice given by Gustavo Pinares has been a great help and his willingness to share his time so generously is very much appreciated.

Special thanks are also extended to the staff of STRI Göteborg for their support and for making my day-to-day at the office more pleasant.

I would also like to acknowledge my friends who have made my time in Sweden so enjoyable, even though they have been often times relegated during the span of this project.

Last but not least, I would like to thank my family for their unconditional support in all my endeavours. All I am, I owe to them.

Omar Juárez Moreno, Gothenburg, June 2017

Contents

List of Figures **xiii**

List of Tables **xvii**

List of Acronyms **xix**

1 Introduction **1**
1.1 Background and motivations 1
1.2 Aim and scope 2
1.3 Structure of the thesis 3

2 Basic Concepts **5**
2.1 The Nordic power system 5
2.1.1 Nordic32A bus system 6
2.2 Frequency dynamics 7
2.3 Ancillary services 8
2.4 Operational reserves 8
2.4.1 Primary, secondary and tertiary reserves 8
2.4.2 Reserve products in the Nordic power system 9
2.4.3 Other frequency-control actions in the Nordic power system . 9
2.5 Energy storage in power systems 10
2.5.1 Basic layout of a ESS 10
2.6 Battery energy storage systems 11
2.6.1 Batteries 12
2.6.2 Battery management systems 12
2.7 Voltage source converters 13
2.7.1 Limiting strategies 14

3 Design of the proposed ancillary service **15**
3.1 System layout 15
3.2 Control strategy for the VSC 16
3.3 PLL 17
3.4 Inner current control loop 17
3.4.1 One-degree-of-freedom controller design 18
3.4.2 Improved current controller 20
3.4.3 Analysis of the current controller 22
3.5 Voltage limiter 23

3.6 Reference calculation . . . 23
3.7 Implementation of a current limiter . . . 24
3.8 Derivation of anti-windup function for the integrator . . . 25
3.9 Outer controllers . . . 26
3.9.1 Frequency controller . . . 26
3.9.2 AC voltage controller . . . 27
3.10 Battery . . . 27
3.11 Battery management system . . . 30

4 Implementation and model verification 33
4.1 Implementation approach . . . 33
4.1.1 RMS and EMT simulations . . . 33
4.1.2 Model revision . . . 34
4.1.3 Model evaluation . . . 35
4.2 VSC control . . . 36
4.3 Current controller . . . 38
4.3.1 Basic current controller . . . 38
4.3.2 Improved current controller . . . 40
4.3.3 Current controller analysis . . . 42
4.3.4 Sensitivity to parameter variations . . . 43
4.3.4.1 Sensitivity to variations in the filter inductance . . . 43
4.3.4.2 Sensitivity to variations in the filter resistance . . . 44
4.4 Frequency controller . . . 46
4.5 Current limiter . . . 47
4.6 Battery . . . 48
4.7 BMS . . . 50

5 Results from application study 53
5.1 Test scenario . . . 53
5.2 Frequency dip after 750 MW of generation is tripped . . . 54
5.3 Different converter ratings . . . 55
5.4 Decommissioning of thermal plants in the Southwest zone . . . 58

6 Discussion 61
6.1 Sustainable development . . . 61
6.2 Areas of opportunity . . . 61

7 Conclusions 63

Bibliography 65

A Per-Unit values I

B Transformations for three-phase systems III
B.1 Transformation of three-phase quantities into vectors . . . III
B.2 Transformation between fixed and rotating coordinate systems . . . IV

C Nordic32A VII

C.1 PowerFactory implementation VII
C.2 Load flow LF32_028 results VIII

List of Figures

1.1 Evolution of frequency deviation outside 49.90 – 50.10 Hz in the Nordic power system (ENTSO-E, 2016) 1

2.1 Map showing the conforming countries of the Nordic power system . . 5
2.2 Nodal distribution of the buses in the Nordic32 system over Scandinavia. Zone "External" is coloured red, zone "North" is shown in blue, zone "Central" is delineated in black and zone "Southwest" is depicted in magenta. The voltage level of each bus can be discerned by the first number of the bus in question, *i.e.* 400 kV, 220 kV and 130 kV buses begin with 4,2 and 1 respectively 6
2.3 Changes in primary, secondary and tertiary reserves following a severe disturbance (Bohlen and Hassan, 2011) 8
2.4 Frequency controlled actions in the Nordic synchronous system (ENTSO-E, 2016) 10
2.5 Value of energy storage applications (EPRI, 2010) 11
2.6 General control strategy for a grid-connected battery system (Lawder *et al*, 2014) 13
2.7 Three-phase, two-level bridge inverter with a battery as the energy source 14
2.8 Different limitation strategies 14

3.1 Three-phase two-level voltage source converter connected to the grid through a filter reactor 15
3.2 Main block diagram of the control system 16
3.3 Single line diagram of a three-phase SRF-PLL. Dashed lines indicated time-varying signals 17
3.4 Single line diagram of a battery storage system connected to the grid via a voltage source converter and a filter 17
3.5 Closed-loop block diagram of the basic current controller showing the control block $F_c(s)$ and the system block $G_c(s)$ 19
3.6 Addition of active damping, together with a decoupling term through a feed-forward loop and the incorporation of the grid voltage to the current controller. $G'_c(s)$ represents the modified process transfer function, over which the controller $F_c(s)$ acts. $G_c(s)$ remains actual process transfer function. $\underline{v}'_c(s)$ is the modified control signal after the addition of the feed forward terms 21
3.7 Voltage limiter implementation at the output of the current controller 23

3.8 Current limiting strategy that prioritizes the d component and relegates the q component to the remaining capacity of the inverter . . . 24
3.9 Depiction of an anti-windup function for the real component of the current controller. Dashed lines indicate back-calculation paths for the modified error signal of the integrator 25
3.10 Block diagram of the frequency controller consisting of a proportional gain and a droop 26
3.11 Elements of the voltage AC outer controller 27
3.12 Simple battery model consisting only of a resistance in series with an ideal voltage source 28
3.13 Dynamic battery model which uses a non-linear equation to control the voltage source 28
3.14 Typical discharge curve of a 3.5 V, 1 A h Li-Ion battery for a 10C discharge rate. $E_0 = 3.7348$, $K = 0.00876$, $Q = 1$, $A = 0.468$, $B = 3.5294$, $R = 0.09$. 29
3.15 Diagram showing a dynamic battery model with charge and discharge capabilities. It uses a non-linear voltage source dependent on the current and the integrated current flowing trough the battery 29
3.16 K_{soc} droop characteristics 30

4.1 Single-line diagram of a simple test grid consisting of a controllable AC voltage source and a static generator representing the BESS . . . 35
4.2 Built-in current controller for the static generator (DIgSILENT, 2016) 36
4.3 PowerFactory implementation of the control system of the Battery-based proposed ancillary service 36
4.4 PowerFactory implementation of a one-degree-of-freedom current controller with decoupling term 38
4.5 Basic current controller response after a 1 *p.u.* step in the d current is applied at 500 ms 39
4.6 Controller currents response to set-point changes in the basic current controller from Figure 4.4 with decoupling term only 39
4.7 PowerFactory implementation of an improved current controller with feed-forward of the grid voltage, decoupling term, active-damping and an integrator anti-windup function 40
4.8 Current controller with added active damping response compared to a basic current controller after a 1 *p.u.* step in the d current is applied at 500 ms 41
4.9 Comparison of the currents response to set-point changes between a basic current controller and an improved current controller with active damping 41
4.10 Analysis of the current controller with (green) and without (black) active damping. Pole placement is plotted in the complex plane and magnitude and phase margins in Bode plots. Note that the frequency axis units in Bode plots are in *p.u.* 42
4.11 Pole-zero maps of the system's behaviour with an error in the estimation of the filter inductance $\hat{L_f}$ 43

4.12 Oscillations in the current response to a unitary step and decoupling not working due to an under estimation of the estimated filter inductance $\hat{L_f} = 0.1L_f$ 44
4.13 Pole-zero maps of the system's behaviour with an error in the estimation of the filter inductance $\hat{R_f}$ 45
4.14 Overshoot in the d current response due to an over estimation of the filter resistance $\hat{R_f} = 10R_f$ 45
4.15 PowerFactory implementation of the outer frequency controller 46
4.16 Frequency controller signals illustrating the effect of the filter acting on the frequency input and the dead-band 47
4.17 Current limiter giving preference to the d component of the current . 48
4.18 PowerFactory implementation of a dynamic battery model with charge/discharge capabilities 49
4.19 Nominal voltage discharge characteristic at different C rates for a 3.3 V, 2.3 A h Li-Ion battery. $E_0 = 3.366, R = 0.01, K = 0.0076, A = 0.26422, B = 26.5487$ 49
4.20 Battery's states of a 3.3 V, 2.3 A h Li-Ion battery when subjected to charge/discharge cycles. $E_0 = 3.366, R = 0.01, K = 0.0076, A = 0.26422, B = 26.5487, C_{rate} = 10$ 50
4.21 3.3 V, 2.3 A h Li-Ion battery state of charge, K_{soc} droop component and nominal discharge curve.$E_0 = 3.366, R = 0.01, K = 0.0076, A = 0.26422, B = 26.5487, C_{rate} = 10$ 51

5.1 Frequency measurement showing the action of the BESS after 750 MW of generation is tripped. The right plot is a zoom of the frequency Nadir. 50 MW, 300 MWh BESS 54
5.2 Frequency measurements for the base case and BESS compensated scenario after the loss of 750 MW of generation juxtaposed with the power measurements from the BESS. 50 MW, 300 MWh BESS . . . 55
5.3 Battery states of a a 50 MW, 300 MWh BESS after the loss of 750 MW of generation 56
5.4 Frequency measurements comparing the effect of converter rating for the same frequency event caused by the loss of 300 MW of generation 56
5.5 Power and SOC measurements comparing the effect of converter rating for the same frequency event caused by the loss of 300 MW of generation 57
5.6 Decommissioning of generators G4062, G4063_1 and G4063_2 for wind farms with the same power output in the Southwest zone 58
5.7 Frequency measurements after the loss of 300 MW of generation. The blue line represents the case were a part of the thermal generation has been replaced by wind power. The right plot is a zoom of the frequency Nadir 59
5.8 Frequency measurements for a 300 MW loss of generation. The right plot is a zoom of the frequency Nadir. 50 MW, 300 MWh BESS . . . 60

5.9 Frequency measurements for a 300 MW loss of generation in the case where nuclear has been replaced by wind power. The right plot is a zoom of the frequency Nadir. 50 MW, 300 MWh BESS 60

B.1 Two sample vectors, $\underline{v}$(t) and $\underline{u}$(t), rotating in the positive sequence with constant frequency in the fixed reference frame $\alpha\beta$ IV
B.2 Relation between the stationary $\alpha\beta$ reference frame and the rotating dq reference frame. Vector $\underline{u}$(t) is taken as reference for the d axis . . V

C.1 PowerFactory single-line diagram of the Nordic 32 bus system showing the results of the load flow LF23_28 with high transfers VII
C.2 PowerFactory output displaying the results of the load flow LF23_28 with high transfers VIII

List of Tables

5.1 System data from load flow LF32_028 (Svenska kraftnät, 1993) . . . 53
5.2 Ratings and inertias (Svenska kraftnät, 1993) 53

List of Acronyms

aFRR Automatic Frequency Restoration Reserves.
AS Ancillary Service.
BESS Battery Energy Storage System.
BMS Battery Management System.
BOP Balance of Plant.
ESS Energy Storage Systems.
FCR Frequency Containment Reserves.
FCR-D Frequency Containment Reserve for Disturbance operation.
FCR-N Frequency Containment Reserve for Normal Operation.
FRR Frequency Restoration Reserves.
mFRR Manual Frequency Restoration Reserves.
PCS Power Conversion System.
PLL Phase Locked Loop.
SOC State of Charge.
SRF-PLL Synchronous Reference Frame Phase-Locked Loop.
TSO Transmission System Operators.
VSC Voltage Source Converter.

1
Introduction

This chapter provides the background and motivations for the realization of this thesis. It also outlines the structure of the chapters contained in the report.

1.1 Background and motivations

The power system is constantly subjected to all kinds of disturbances. The severity of the these can range from minor disturbances such as the constant changes in the load condition, to acute ones, like a fault leading to the loss a large generating unit. These events are usually reflected in deviations in the frequency. In order to maintain an acceptable level of quality, ENTSO-E has defined the highest permissible frequency variation for the Nordic power system to be between 49.90 and 50.10 Hz [1]. The adherence to this standard is measured by the number of minutes that the system exceeds is outside the normal frequency operation band.

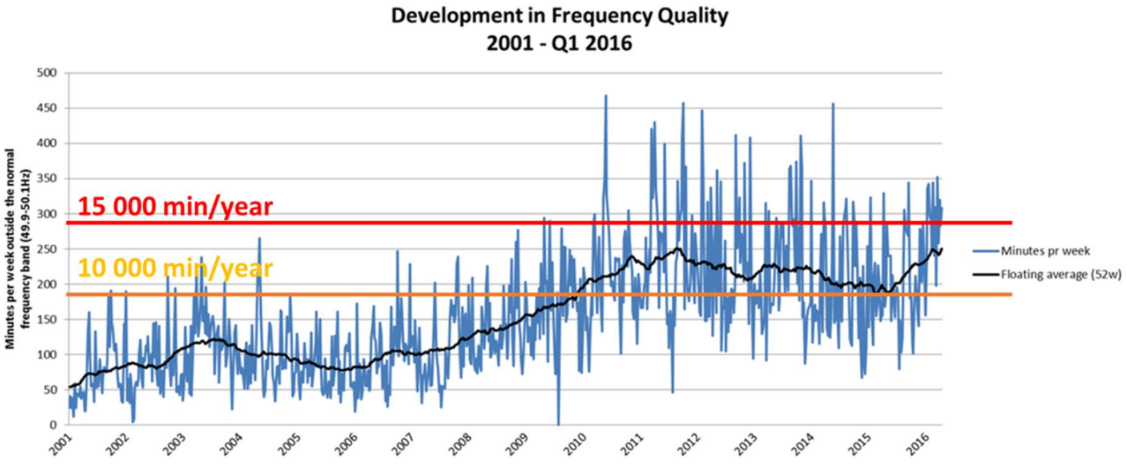

Figure 1.1: Evolution of frequency deviation outside 49.90 – 50.10 Hz in the Nordic power system (ENTSO-E, 2016)

According to [1], the goal for frequency deviations outside normal frequency band shot not be more than 10 000 min/year. However, in recent years, the number of minutes outside the permissible range for normal operation has increased. Figure 1.1 shows the trend of frequency quality in the Nordic power system from 2001 to 2016. It could be argued, that this trend is expected to continue, specially with the current tendency to replace conventional generation with intermittent, renewable

energy sources (RES) that are decoupled from the grid.

On that account, the future of the power system has been envisioned as a *Smart Grid* [2]. A Smart Grid can be defined as an electricity network that can intelligently integrate the actions of all users connected to it, in order to efficiently deliver sustainable, economic and secure electricity supplies [3]. This vision has lead to the introduction of newer products and AS with the objective of facilitating the implementation of renewable energy sources, while at the same time, ensuring the security and reliability of the system [4].

Traditionally, Transmission System Operators (TSO) have made use of generators and, recently, of flexible loads and FACTS devices, to provide AS to the grid. However; nowadays, the Smart Grid framework also allows the possibility to use network connected devices, such as batteries, as ancillary service providers [5].

The joint programming initiative ERA-Net Smart Grids Plus has provided funding for the research project "CloudGRid", which aims to develop the smart grid concept in the interconnected European power system. The project is divided into six Work Packages (WP), from which WP5 deals with Ancillary Services and Energy Management. WP5 primary objective is to explore opportunities to support the system through additional ancillary service solutions and novel strategies for energy management. This thesis was carried out within the frame of WP5, during a period of 6 months, from January to June 2017, at STRI AB in Gothenburg, Sweden.

1.2 Aim and scope

The aim of the thesis is to develop a model of a battery storage system to be used as a frequency support ancillary service in the Nordic power system.

The focus of the thesis is to study the effect that a battery storage system providing frequency support can have on enhancing the robustness of the power system. This means that the main interest of the thesis is the action of the system as a whole and not the detailed modelling of the individual components that make up the system. The network will be assumed to be in steady state and only balanced faults/trippings will be applied to provoke a frequency event. No consideration is given to thermals or losses, therefore, no efficiency evaluation is provided. Since the aim of the model is to provide frequency support, only the frequency measurements and battery states will be pondered for the evaluation and results. Transient and voltage stability were not considered when performing dynamic simulations.

1.3 Structure of the thesis

The outline of the thesis is as follows:

Chapter 1 introduces the thesis' background and motivations.

Chapter 2 equips the reader with basic concepts that provide a solid foundation about the thesis' field of study.

Chapter 3 describes in detail the development and derivation of the models used in the proposed ancillary service.

Chapter 4 presents the implementation approach and validation of the derived models.

Chapter 5 reports the results obtained from the study case.

Chapter 6 proposes a discussion on the possible environmental impacts that such a system would have and also puts forward possibilities to expand the work presented in this thesis.

Chapter 7 draws up the conclusions of the thesis.

2
Basic Concepts

This chapter intends to acquaint the reader with the basic basic concepts needed to understand the background of the thesis.

2.1 The Nordic power system

Figure 2.1 shows a map over Scandinavia. In the Nordic countries, production systems differ greatly from one country to another. Denmark uses conventional thermal power and an increasing proportion of wind power. Norway has hydropower, whilst Finland and Sweden have a mix of different systems with mostly hydro and nuclear power [6].

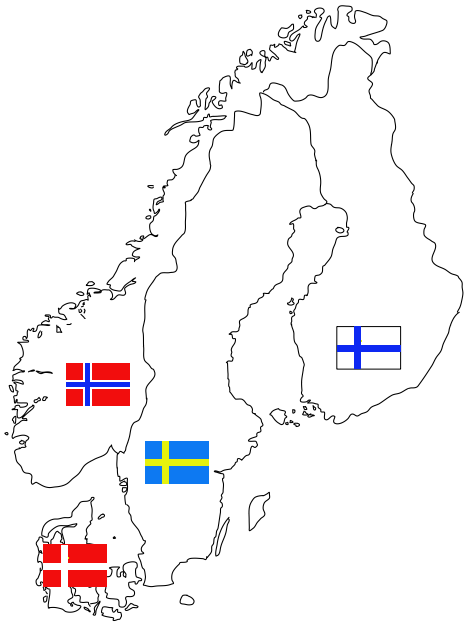

Figure 2.1: Map showing the conforming countries of the Nordic power system

The subsystems in Finland, Norway, Sweden and eastern Denmark are interconnected synchronously and form what is known as the "synchronised system". The subsystem in Western Denmark is connected to Norway and Sweden via HVDC links. Together, the synchronous system and the Western Denmark subsystem form the interconnected Nordic electric power system [6].

2.1.1 Nordic32A bus system

The Nordic32A test power system was developed by CIGRÉ in cooperation with Svenska kraftnät, the Swedish TSO, in 1993. It is intended for transient and long-term stability simulations and consist of 32 buses, 52 lines and 23 generators.

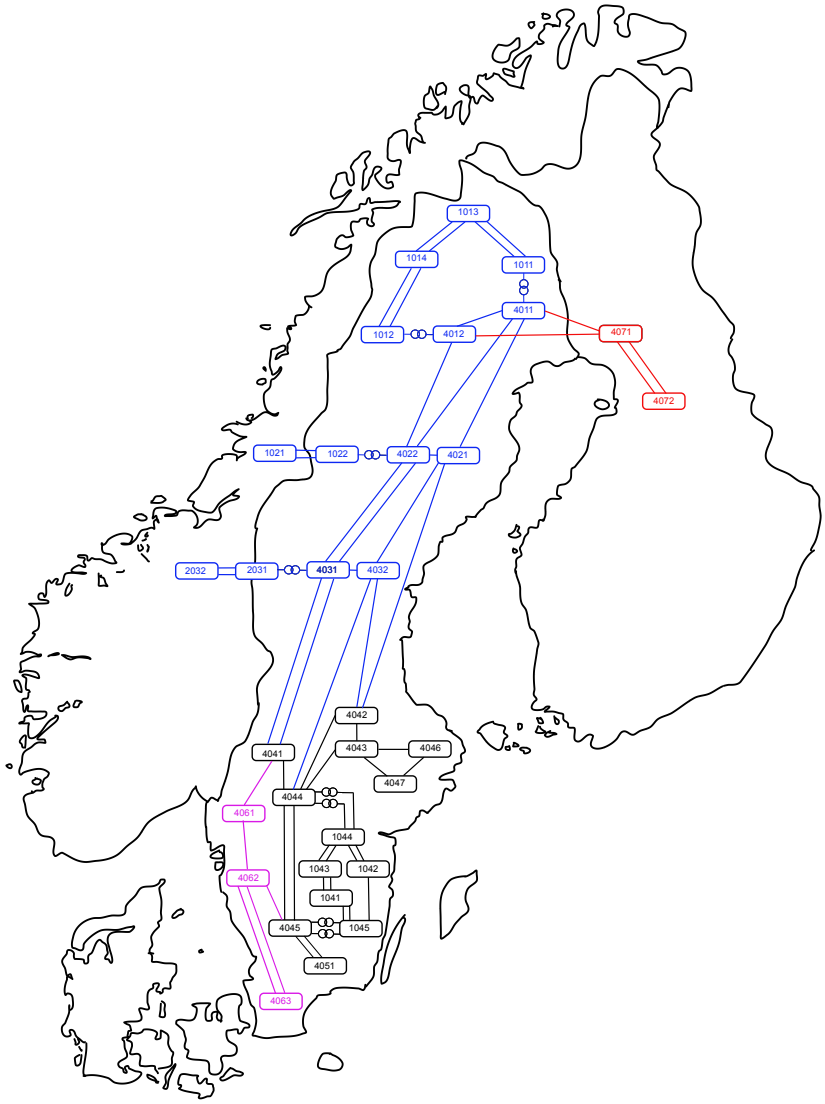

Figure 2.2: Nodal distribution of the buses in the Nordic32 system over Scandinavia. Zone "External" is coloured red, zone "North" is shown in blue, zone "Central" is delineated in black and zone "Southwest" is depicted in magenta. The voltage level of each bus can be discerned by the first number of the bus in question, *i.e.* 400 kV, 220 kV and 130 kV buses begin with 4,2 and 1 respectively

The system is fictitious, but has a distribution and dynamic properties similar to that of the Swedish power system. That is, the system is characterized by large power transfers from a hydro-dominated north zone to a central load zone with large amounts of load and some thermal power [7].

2.2 Frequency dynamics

In an interconnected system, frequency is a global factor. A change in power balance in one part will be reflected as a change of frequency in the whole system [8]. This is the reason why a fundamental part in describing the frequency stability of the system is understanding the relation between the mechanical input of a generator, P_m and the electrical output, P_e. Thus, in steady state the balance between generation and consumption is

$$P_m = P_e \tag{2.1}$$

The rotational energy of the machine is given by

$$E_{rot} = \frac{1}{2} J\omega^2 \tag{2.2}$$

where J is the combined moment of inertia of the generator and the turbine in $\mathrm{kg\,m^2}$ and ω is the angular velocity of the rotor in rad/s. Any unbalance would result in a change in the rotating energy of the machine:

$$\frac{d(E_{rot})}{dt} = P_m - P_e \tag{2.3}$$

Putting (2.2) into (2.3) and calculating the derivative gives

$$\frac{d\omega}{dt} = \frac{P_m - P_e}{J\omega} \tag{2.4}$$

Defining the inertia constant H as the ratio of the rotational energy at nominal speed ω_0 and the total base power S_b:

$$H = \frac{\frac{1}{2} J\omega_0^2}{S_b} \tag{2.5}$$

Now, we can describe J as

$$J = 2H\frac{S_b}{\omega_0^2} \tag{2.6}$$

Inserting (2.6) in (2.4) we get

$$\frac{d\omega}{dt} = \frac{P_m - P_e}{2H\frac{S_b}{\omega_0^2}\omega} \tag{2.7}$$

If we assume a small variation in the rotational speeds, $\omega \cong \omega_0$, then,

$$\frac{d\omega}{dt} = \frac{\omega_0}{2H}\frac{P_m - P_e}{S_b} \tag{2.8}$$

Similarly, if we consider $\omega = 2\pi f$ and $\omega_0 = 2\pi f_0$, then the change in frequency due to unbalance power between P_m and P_e, both in *p.u.* is

$$\frac{df}{dt} = \frac{f_0}{2H}(P_{m\,p.u.} - P_{e\,p.u.}) \tag{2.9}$$

From (2.9), it is evident that the system frequency is dependant on the active power balance. Since there exist many generating units supplying the system, some means must be procured to respond to the change in demand in the system. This is achieved by means of frequency control [8].

2.3 Ancillary services

EURELECTRIC defines Ancillary services as: "All services required by the transmission or distribution system operator to enable them to maintain the integrity and stability of the transmission or distribution system as well as the power quality [9]." The main services in use today are voltage control and frequency control at different time scales and black start capability for system restoration [10].

2.4 Operational reserves

2.4.1 Primary, secondary and tertiary reserves

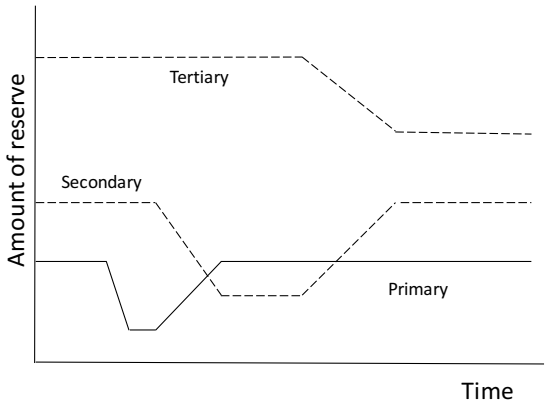

Figure 2.3: Changes in primary, secondary and tertiary reserves following a severe disturbance (Bohlen and Hassan, 2011)

Primary reserves are used to quickly react on frequency deviations and to stabilize frequency. After a short while, the primary reserves are restored by the secondary reserves which in turn, are replaced by the tertiary reserves. This releases the primary and secondary reserves which are, then, again available for the next balancing needs. This is illustrated in Figure 2.3 adapted from [11], where the change in reserve type as a function of time is shown (not to scale). The n-1 criterion is fulfilled for this case. At this point, the customer has not yet been impacted by the disturbance. Only when the magnitude of the disturbance is larger than the primary reserves does the system become unstable.

2.4.2 Reserve products in the Nordic power system

ENTSO-E has laid down clear rules in [10] about the amount of operational reserves and who is responsible for procuring them. Nonetheless, different terminology is used for the types of reserves used in the individual synchronous areas. For the Nordic system, ENTSO-E distinguishes the following reserve products [1]:

- Frequency Containment Reserve for Normal Operation (FCR-N). Is a specific Nordic product with the purpose of balancing the system within the normal frequency band ($49.90 < f < 50.10$ Hz). Since this is within the range of normal operation for the Nordic synchronous area, no sudden changes in production take place and the activation time is rather slow: normally regulated upwards/downwards within 2 min to 3 min.

- Frequency Containment Reserve for Disturbance operation (FCR-D). It has the purpose of stabilizing the system in case of disturbances where frequency drops below 49.9 Hz and it will be completely committed at 49.5 Hz. 50% of the reserve shall be regulated upwards within 5 s and the 100% shall be regulated upwards within 30 s.

- Manual Frequency Restoration Reserves (mFRR) is used for power balancing and to handle congestions in normal and disturbance situations. mFRR is the main balancing resource which when activated replaces both remainingFrequency Containment Reserves (FCR) and aFRR activations and brings frequency back to the frequency target. The required activation time is 15 min.

- Automatic Frequency Restoration Reserves (aFRR) is an automatic complement in the FRR process. The aFRR reserve differs from FCR in that the reserve is remotely controlled by a centralized controller while FCR is locally controlled. An advantage of aFRR over FCR is that it can be based on a merit order and take congestions in the grid into account.

2.4.3 Other frequency-control actions in the Nordic power system

ENTSO-E operation's agreement for the Nordic synchronous area [12], states the following frequency controlled system protection to be activated by a deviating frequency:

- Regulation of DC facilities, emergency power
- Production shedding or downward regulation of production
- Start-up of production
- Automatic load shedding
- Network switchings.

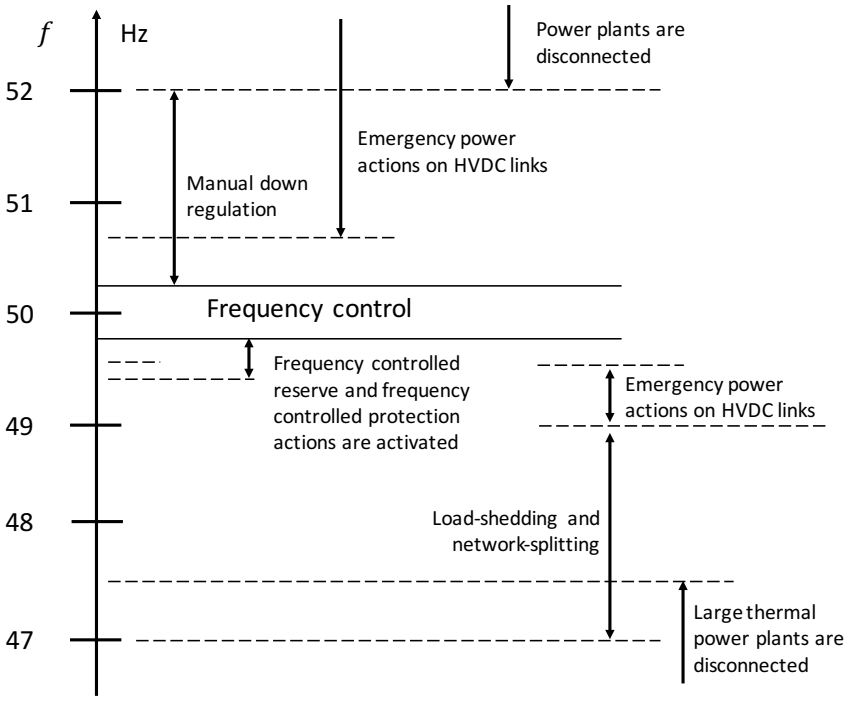

Figure 2.4: Frequency controlled actions in the Nordic synchronous system (ENTSO-E, 2016)

Figure 2.4, adapted from [12], illustrates the actions taken by system operators within the Nordic synchronous area to deal with frequency disturbances.

2.5 Energy storage in power systems

In power systems, Energy Storage Systems (ESS) are energy storage technologies that absorb electrical power during periods of excess capacity so that it can be released later when it has more value. This characteristic makes it possible for ESS providers to supply various types of services to the power grid utility. The possibilities encompass the entire value chain of the electrical system, ranging from generation level and system utilities to end-user applications. In Figure 2.5, EPRI, proposes the following classification of ESS according to their intended application in the value chain [13].

2.5.1 Basic layout of a ESS

Each energy storage unit facility is made up of three distinct components: the storage medium, the Power Conversion System (PCS), and the Balance of Plant (BOP) [14].

The energy storage unit is also commonly referred to as the *energy reservoir* and it

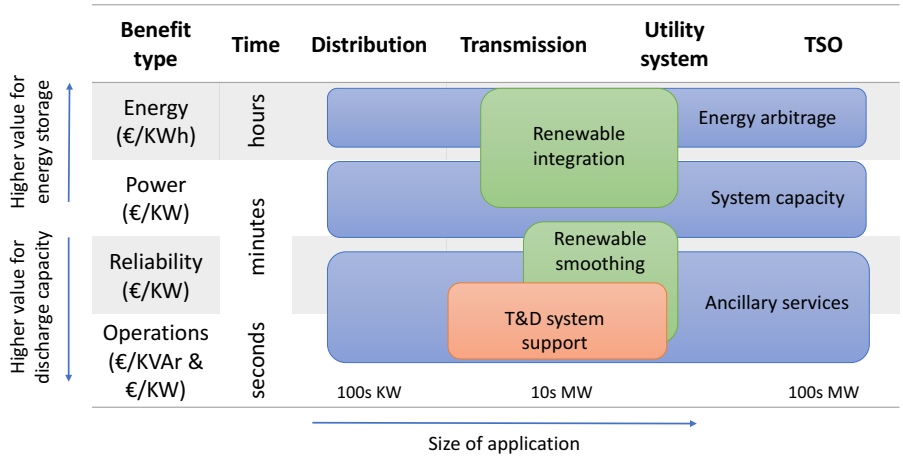

Figure 2.5: Value of energy storage applications (EPRI, 2010)

is the main component of a ESS. The main differentiating factor between them is the form in which the energy is stored. This in turn, influences each technology's operational capabilities and consequently, the application in which it is used for. Of course, even though some technologies center around an specific goal, they are also able to provide multiple benefits. For example, the energy stored can be delivered in large amounts and sold as a commodity. Another possibility is to operate the unit in a controlled charge/discharge cycle in order to dampen fluctuations in the system's power level. However, not all technologies have been developed enough to make them suitable for large-grid scale applications [13].

The PCS is also an integral part of any ESS. It consists of a number of devices and controllers to enable energy conversion from the storage state to the grid-bound state.

Finally, the BOP comprises the auxiliary systems that support the operation of the ESS. BOP typically includes transformers, electrical interconnections, surge protection devices, a support rack for the storage medium and the facility to shelter the unit from the elements [14].

2.6 Battery energy storage systems

While many technologies have been developed for large-scale energy storage purposes such as pumped-hydro storage, compressed-air energy storage or flywheels; many are limited in their site dependence, capacity, or response capabilities. Battery Energy Storage System (BESS) on the other hand offer great flexibility in capacity ratings and a rapid response which is ideal to meet demands over a much wider range of functions than many other types of storage [15].

2.6.1 Batteries

Batteries comprise a wide range of technologies based on the material used in electrodes and electrolytes, and the way they convert chemical energy into electrical energy and *vice versa*. Batteries can be divided into two categories: primary or secondary. Primary batteries are not rechargeable: they are single-use disposable batteries and must be discarded once their charge has been depleted. On the other hand, secondary batteries are rechargeable [16].

When discussing batteries it is valuable to get acquainted with some terminology that is often used. Concepts like Ah, C-rate and State of Charge (SOC) define the operational characteristics of a battery pack. The capacity of a battery is often stated in Ah (Ampere hours). If a battery has a capacity of 5Ah hours, it can deliver 5A for 1 hour or it can deliver 1A for 5 hours.

The amount of energy the battery can deliver is the current multiplied with the voltage and integrated over time. A complicating factor is that the battery terminal voltage varies depending on the amount of current that is delivered to or drawn from the battery. The internal voltage level also depends on the SOC, which is a number between 0 and 1 (or 0-100 %) that tells us how much charge is still left in the battery, such that an SOC of 1 (or 100 %) means that the battery is fully charged. In reality however, it is not possible to use 100% of the battery pack's capacity, only about 80–90% of the capacity of the battery is usable depending on the cell selection and usage profile.

The C-rate describes how fast the battery can be charged or discharged. A 1C discharge rate means that the total battery capacity of the battery will be utilized in 1 hour. If the battery is discharged at a 2C rate, the battery will be emptied in half an hour, and the current drawn will be twice as large as in the 1C case. The total energy content is the pack voltage times the pack ampere hours.

Each battery cell typically holds just a few volts and can deliver only a few Ah. Different battery technologies have different typical ratings. To reach desired battery pack voltage and energy ratings, many cells are combined. By series connecting cells the battery voltage can be increased. If the battery pack's energy content is not enough with one layer of series connected cells, it can be increased by adding one or several parallel layers as well, which increases the battery-pack's capacity.

2.6.2 Battery management systems

The basic task of a Battery Management System (BMS) is to ensure that optimum use is made of the energy inside the battery powering a BESS and that the risk of damage inflicted upon the battery is minimized [17].

BESS require a BMS to keep track of important operational attributes of the battery in order to maintain the unit operating safely and optimally. Batteries are dynamic in nature and their operation is dependent on many factors interrelated to each

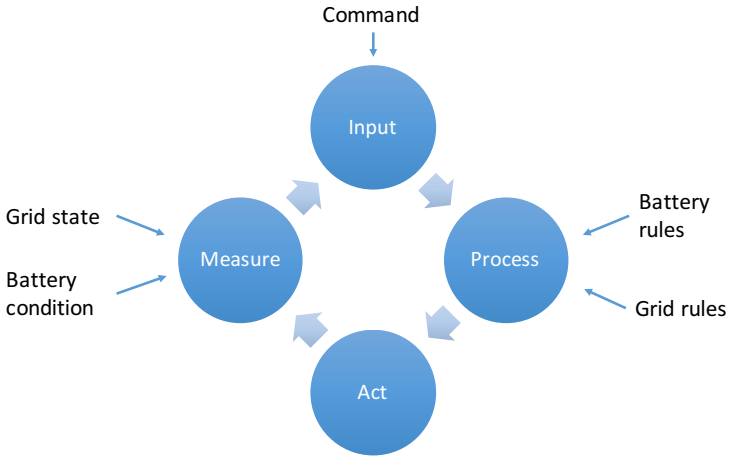

Figure 2.6: General control strategy for a grid-connected battery system (Lawder *et al*, 2014)

other. The most basic BMS controls only the power exchange. However, an integral BMS will also monitor the health of the battery, by keeping track of the temperature gradients across the system, for example. In addition to that, it will also improve the performance of the system by, for instance, providing optimal charging patterns and balancing the cells in the stack. BMS are able to accomplish these functions by manipulating the current and computing it to accurately estimate many internal variables to which it has no access [15].

As a controller, the BMS receives signals from external sources such as commands and measurements, while it calculates the appropriate response to fulfill the action as required by the grid. Figure 2.6 illustrates a general control strategy for grid-connected BESS proposed in [15]. In short, it can be said that the BMS is responsible for safe operation of the BESS: making sure that it operates within thermal and safe voltage and current limits; and for state estimation of the SOC among others.

2.7 Voltage source converters

Three-phase inverters are power electronic devices that convert a DC voltage into an AC voltage. They are used when the objective is to produce a sinusoidal output voltage with a controllable magnitude and frequency. There exist many possible configurations, but the most widely used to feed AC power supplies or motor drives consists of three legs, one for each phase. A schematic of the device is shown in Figure 2.7. Two equal capacitors are connected in series in parallel to the DC output of the energy storage medium [18].

The output voltage $u_c(t)$ of each leg depends only on the DC voltage of the converter $u_{dc}(t)$ and the status of the switch $T\pm$. The converter switches are usually IGBT semiconductors in an anti-parallel diode, $D\pm$, arrangement [18].

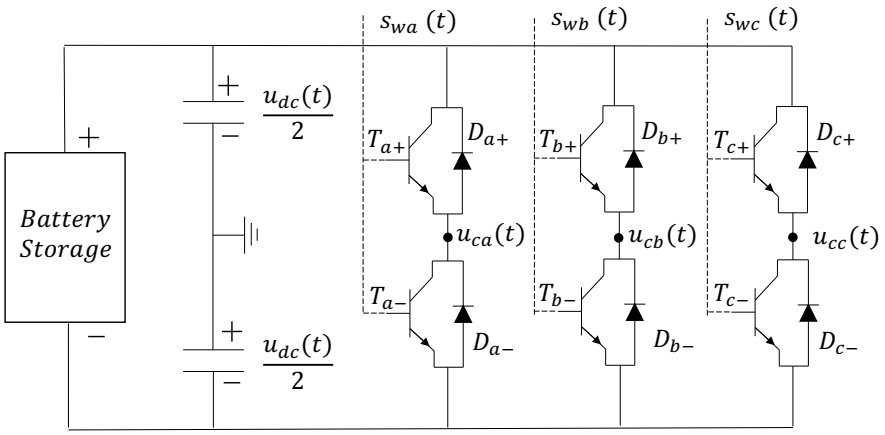

Figure 2.7: Three-phase, two-level bridge inverter with a battery as the energy source

2.7.1 Limiting strategies

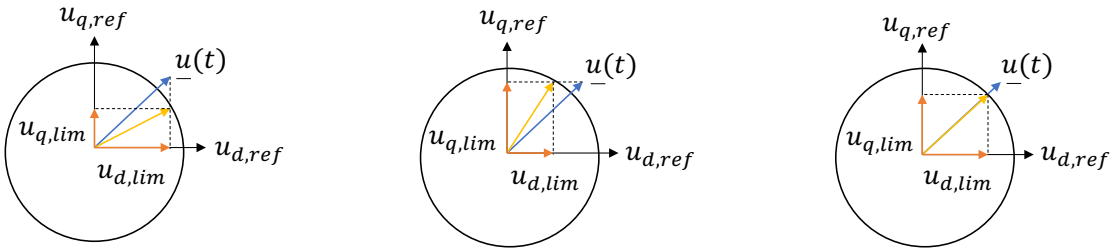

Figure 2.8: Different limitation strategies

As opposed to electromechanical devices such as motors and generators, solid-state components do not have any inherent overload capability. In the case of a VSC, it may occur that some events demand a response that exceeds the rating of the converter, thus damaging the device. This is the reason why current and voltage limiters are implemented in the control system of a VSC.

Basically, three different types of limitations exist [19]. Taking the vector $\underline{u}(t)$ in the synchronous dq reference frame as an example, these limiting strategies are visualized in Figure 2.8. One can choose to prioritize one component over the other, at the expense of affecting the angle of the resulting limited vector, while it is also possible to limit the magnitudes of the vectors and to keep the reference angle intact.

3

Design of the proposed ancillary service

This chapter contains a detailed description of the derivation of the models that make up the proposed ancillary service.

3.1 System layout

Figure 3.1 depicts the schematics of a battery interfaced to the grid via a VSC through a filter reactor composed of an inductance L_f in series with a resistance R_f. The reactor serves as filter to reduce high switching harmonics due to the switching of the VSC and also to limit short-circuit currents in the event of a fault [8]. The VSC injects the currents $i_{fa}(t), i_{fb}(t)$ and $i_{fc}(t)$. The points of connection to the grid for the three legs of the converter are $e_{ga}(t), e_{gb}(t)$ and $e_{gc}(t)$ respectively. The grid impedance is represented by the terms L_g and R_g.

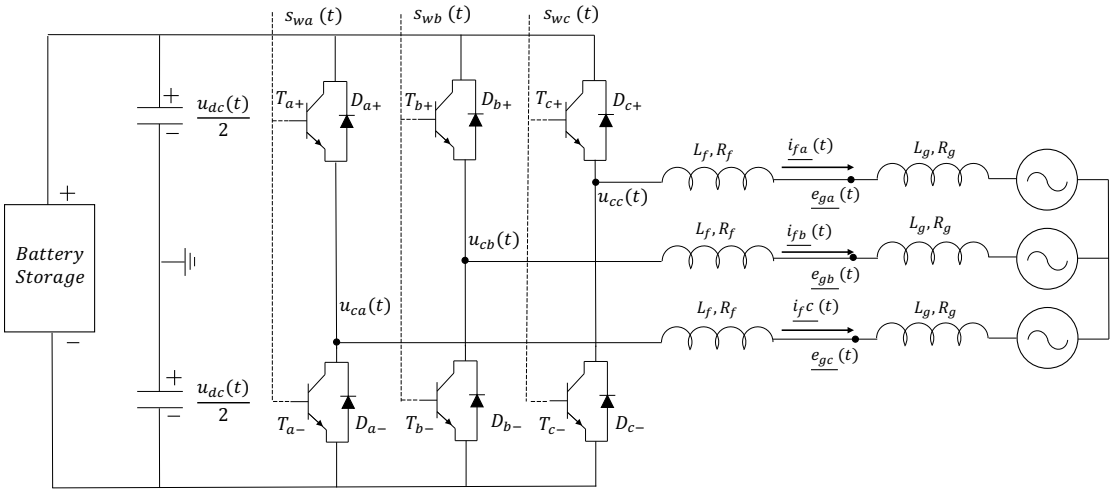

Figure 3.1: Three-phase two-level voltage source converter connected to the grid through a filter reactor

3.2 Control strategy for the VSC

The block diagram presented in Figure 3.2 illustrates the proposed control strategy for the grid connected VSC from Figure 3.1. Voltage and current measurements from the grid connection point are rotated from three-phase quantities to the dq synchronous reference frame. The system uses a SRF-PLL in order to track the phase angle $\theta(k)$ used for the coordinate transformation blocks, where (k) stands for the sample index. The battery storage system is controlled by an IMC inner current control loop. The BMS receives the SOC information from the battery and computes it in the form of a droop component K_{soc}. This droop, together with the frequency measurement from the PLL, is used by the outer frequency controller to output the active power reference. The reactive power reference is obtained from the outer voltage controller. Current and voltage limiter blocks are implemented at the output of the set-point changers in order to restrict the system's response to the physical limits of the VSC. The control algorithm provides the switching signals $s_{wa}(k)$, $s_{wb}(k)$ and $s_{wc}(k)$ to be used as reference for the PWM that drives the valves of the three-phase, two-level inverter.

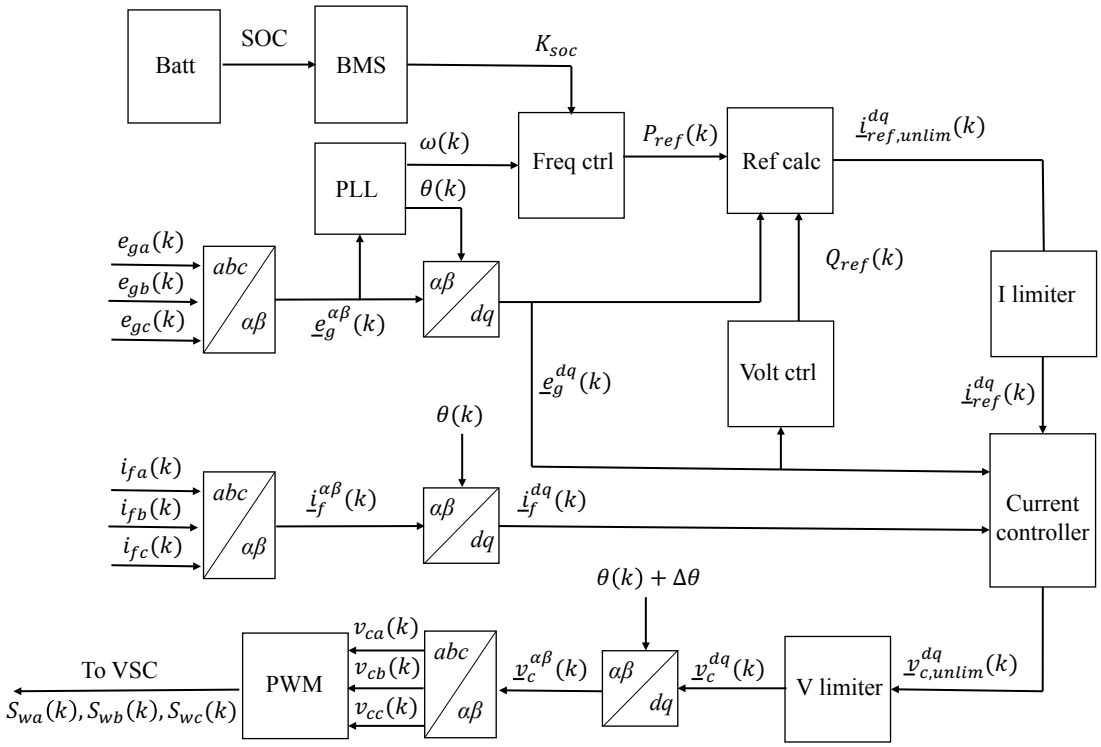

Figure 3.2: Main block diagram of the control system

In the $dq/\alpha\beta$ transformation block at the output of the voltage limiter, a compensation angle $\Delta\theta = 1.5\omega T_s$, where T_s stands for sampling time, is added to take into account the one and a half sample delay introduced by the discretization of the measured quantities.

The derivation of the different control blocks will be described in detail in the following sections.

3.3 PLL

Many implementations of the PLL exist for both one-phase and three-phase applications. However, the most widely used form of PLL in the areas of electric power engineering is the SRF-PLL [20].

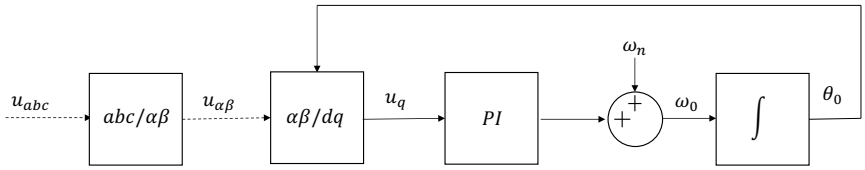

Figure 3.3: Single line diagram of a three-phase SRF-PLL. Dashed lines indicated time-varying signals

Figure 3.3 shows the single line diagram of a SRF-PLL. The input signal is a three-phase quantity, usually the voltage. It is transformed into a two-phase representation in the static reference frame $\alpha\beta$. For information on coordinate transformations for three-phase systems, refer to Appendix B. The resulting signal is still a time-varying complex quantity composed of a real component α and and imaginary component β. Then, the dq signals can be computed using the phase angle and the projection matrix described in Appendix B. Assuming that the output frequency is equal to the input frequency, u_{dq} is constant with no double-frequency oscillations. By regulating u_q to 0, the SRF-PLL regulates the output phase angle θ_0 to the input angle θ_i. Consequently, by regulating u_q to 0, u_d is regulated to the input signal's magnitude [20].

3.4 Inner current control loop

In order to facilitate the analysis, the circuit presented in Figure 3.1 can be simplified to a single line diagram such as the one presented in Figure 3.4, which is composed of the same elements and represents the same dynamics.

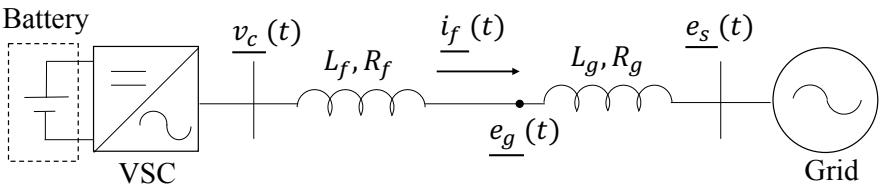

Figure 3.4: Single line diagram of a battery storage system connected to the grid via a voltage source converter and a filter

Taking as reference Figure 3.4, the dynamics of the current $\underline{i}_f(t)$ flowing through the reactor, in $\alpha\beta$, are

$$L_f \frac{d}{dt}\underline{i}_f^{\alpha\beta}(t) = \underline{v}_c^{\alpha\beta}(t) - \underline{e}_g^{\alpha\beta}(t) - R_f\underline{i}_f^{\alpha\beta}(t) \tag{3.1}$$

By adding the phase angle $\theta(t)$ to the $\alpha\beta$ quantities, a rotation with the same system frequency is incorporated to the vectors, effectively making them appear static in the dq frame.

$$\underline{v}^{\alpha\beta}(t) = \underline{v}^{dq}(t)e^{j\theta(t)} \tag{3.2}$$

After inserting it to all of the terms, equation (3.1) will transform into

$$L_f \frac{d}{dt}\underline{i}_f^{\alpha\beta}(t)e^{j\theta(t)} = \underline{v}_c^{\alpha\beta}(t)e^{j\theta(t)} - \underline{e}_g^{\alpha\beta}(t)e^{j\theta(t)} - R_f\underline{i}_f^{\alpha\beta}(t)e^{j\theta(t)} \tag{3.3}$$

Simplifying yields the current dynamics in the dq reference frame. For clarity purposes, no indexes will be used for the complex dq values.

$$L_f \frac{d}{dt}\underline{i}_f(t) = \underline{v}_c(t) - \underline{e}_g(t) - R_f\underline{i}_f(t) - j\omega L_f\underline{i}_f(t) \tag{3.4}$$

Arranging the terms yields the voltage expression $\underline{v}_c(t)$ in terms of the current $\underline{i}_f(t)$ and the additional grid voltage term $\underline{e}_g(s)$.

$$\underline{v}_c(t) = L_f \frac{d}{dt}\underline{i}_f(t) + \underline{e}_g(t) + (R_f + j\omega L_f)\underline{i}_f(t) \tag{3.5}$$

Taking the Laplace transform,

$$\underline{v}_c(s) = sL_f\,\underline{i}_f(s) + \underline{e}_g(s) + (R_f + j\omega L_f)\underline{i}_f(s) \tag{3.6}$$

3.4.1 One-degree-of-freedom controller design

Arranging equation (3.6) as a function of the output over the input, the transfer function $G_c(s)$ of the system's process is obtained.

$$G_c(s) = \frac{\underline{i}_f(s)}{\underline{v}_c(s) - \underline{e}_g(s)} = \frac{1}{sL_f + R_f + j\omega L_f} \tag{3.7}$$

Figure 3.5 depicts a graphical configuration of a closed-loop control system consisting of a controller $F_c(s)$ and the process $G_c(s)$. The controller transfer function $F_c(s)$ is connected in series. Since the controller operates with only one input, the error signal $\underline{e}$, it is said that it is working with only one degree of freedom.

The transfer function of the control system illustrated in Figure 3.5 can be obtained through block algebra and is defined as

$$C(s) = \frac{F_c(s)G_c(s)}{1 + F_c(s)G_c(s)} \tag{3.8}$$

The term $j\omega L_f\underline{i}_f(s)$ is a coupling term introduced by the coordinate transformation and the grid voltage, $\underline{e}_g(s)$, can be considered as a disturbance. Both terms will be

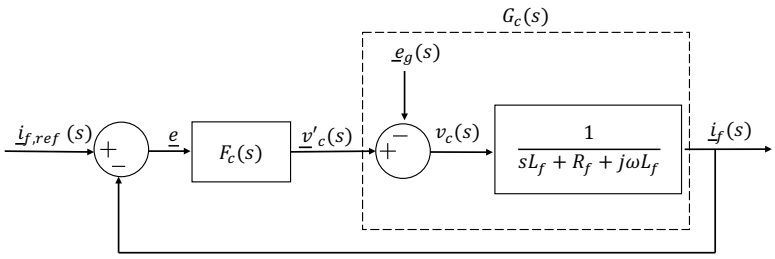

Figure 3.5: Closed-loop block diagram of the basic current controller showing the control block $F_c(s)$ and the system block $G_c(s)$

removed by cross-coupling compensation and a feed-forward term, respectively. As a result, the process transfer function $G_c(s)$ from equation (3.7) can be reduced to a equivalent transfer function $G''_c(s)$, where

$$G''_c(s) = \frac{\underline{i}_f(s)}{\underline{v}_c(s)} = \frac{1}{sL_f + R_f} \tag{3.9}$$

Since the parameters of the process are known, they could be used to select appropriate values for the controller's terms. A good approach is to use this knowledge to shape the response of the system with a method called *loop-shaping*. Electrical dynamics are of order one, so a simple PI controller can provide good performance with a simple arrangement [21]. Consequently, the approximation is made to shape the control system transfer function $C(s)$ to a first order system of the form

$$H_c(s) = \frac{\alpha_c}{s + \alpha_c} = \frac{\alpha_c/s}{1 + \alpha_c/s} = \frac{1}{sT_c + 1} \tag{3.10}$$

where T_c is the process time constant and α_c is the closed-loop bandwidth in $rads/s$ linked to the system's response rise time T_{re} by the relation

$$\alpha_c T_{re} = ln(9) \tag{3.11}$$

Then, considering $G''_c(s)$ defined in (3.9) as the process function, the approximation is made as

$$C(s) = \frac{\alpha_c/s}{1 + \alpha_c/s} \tag{3.12}$$

$$\frac{F_c(s)G''_c(s)}{1 + F_c(s)G''_c(s)} = \frac{\alpha_c/s}{1 + \alpha_c/s} \tag{3.13}$$

Equating both numerators from equation (3.13) gives

$$F_c(s)G''_c(s) = \frac{\alpha_c}{s} \tag{3.14}$$

Then, considering that $F_c(s)$ is a PI controller, the parameters Kp_c, proportional gain and the integrator gain, Ki_c, can be found as

$$F_c(s) = \frac{\alpha_c}{s} G_c''(s)^{-1} \tag{3.15}$$

$$Kp_c + \frac{Ki_c}{s} = \frac{\alpha_c}{s}(s\hat{L_f} + \hat{R_f}) \tag{3.16}$$

which finally yields

$$Kp_c = \alpha_c \hat{L_f};\ Ki_c = \alpha_c \hat{R_f} \tag{3.17}$$

where the tilde "hat" indicates estimated values which should be as close as possible to the actual process parameters.

3.4.2 Improved current controller

The current controller derived in section 3.4.1 is not very robust since it has only one degree of freedom. Moreover, the currents are coupled, which means that a step in one component will have an effect on the other. This is not desirable since it gives poor set-point following. Moreover, the grid voltage $\underline{e}_g(s)$ is constantly acting as a disturbance, which means that any perturbation on the grid voltage will impact the performance of the controller.

It is possible to tackle the aforementioned issues by feed-forwarding another loop to the control signal, thus giving the controller two degrees of freedom. To begin, the grid voltage signal $\underline{e}_g(s)$ will be added in order to cancel out the disturbance in the process transfer function $G_c(s)$, linearizing the the model. Next up, a decoupling term $j\omega\hat{L_f}\ \underline{i}_f(s)$ will be feed-forwarded. These two actions will immediately improve the performance of the current controller, specially the introduction of the decoupling term.

Additionally, it is also possible to include an "active damping" term in the feed-forward loop in order improve the system's disturbance rejection and improve its robustness. The resistive term in the filter reactor provides damping to the controllers response. However, adding more resistance would cause unnecessary losses. The solution is to add a "virtual" resistance R_a to the internal model process of the controller. These actions are illustrated on Figure 3.6, where an improved version of the current controller is shown.

Analyzing both sides of the modified control signal $\underline{v}_c'(s)$ as shown on Figure 3.6 and comparing the expressions gives that

$$\underline{v}_c'(s) = (sL_f + R_f + j\omega L_f)\underline{i}_f(s) + \underline{e}_g(s) \tag{3.18}$$

$$\underline{v}_c'(s) = \underline{v}_c(s) + (j\omega\hat{L_f} + R_a)\underline{i}_f(s) + \underline{e}_g(s) \tag{3.19}$$

Equating both expressions and simplifying gives

$$\underline{v}_c'(s) = \underline{v}_c'(s) \tag{3.20}$$

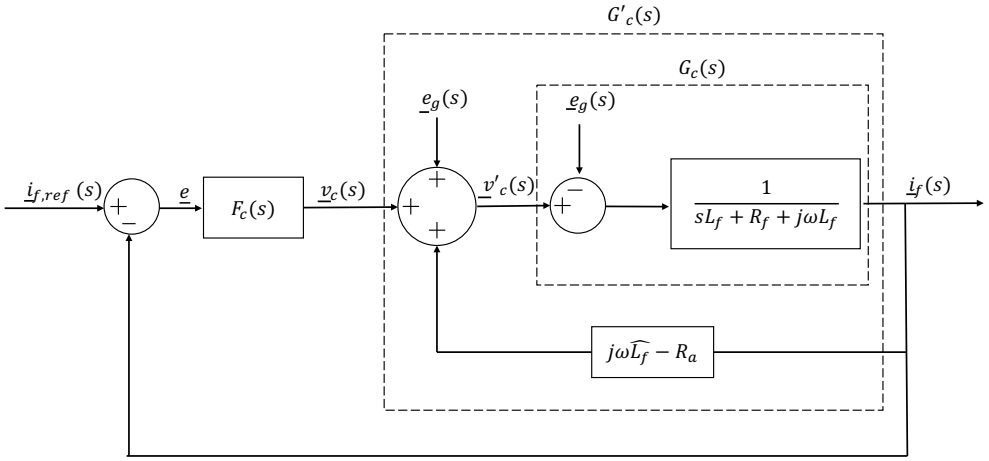

Figure 3.6: Addition of active damping, together with a decoupling term through a feed-forward loop and the incorporation of the grid voltage to the current controller. $G'_c(s)$ represents the modified process transfer function, over which the controller $F_c(s)$ acts. $G_c(s)$ remains actual process transfer function. $\underline{v}'_c(s)$ is the modified control signal after the addition of the feed forward terms

$$(sL_f + R_f)\underline{i}_f(s) = \underline{v}_c(s) + R_a\underline{i}_f(s)$$

where a new process transfer function $G''_c(s)$ can be defined as

$$G''_c(s) = \frac{\underline{i}_f(s)}{\underline{v}_c(s)} = \frac{1}{sL_f + R_f + R_a} = \frac{\alpha_c}{s + \alpha_c} \tag{3.21}$$

The assumption is made again to approximate $G''_c(s)$ to a first order system of the type defined in equation (3.10).

In order to avoid impacting the behaviour of the controller with the added term, it is imperative to give the added term R_a the same process bandwidth α_c. For this purpose,

$$\alpha_c = \frac{\hat{R_f} + R_a}{\hat{L_f}} \tag{3.22}$$

where the parameters are now the estimated values denoted by the tilde "hat" and where the value of R_a is calculated as

$$R_a = \alpha_c\hat{L_f} - \hat{R_f} \tag{3.23}$$

Following the same procedure as in section 3.4.1, equations (3.13) and (3.14), the new controller parameters can be found.

$$F_c(s) = \frac{\alpha_c}{s}\, G'_c(s)^{-1} = \frac{\alpha_c}{s}(s\hat{L_f} + \hat{R_f} + R_a) \tag{3.24}$$

$$Kp_c = \alpha_c\hat{L_f};\; Ki_c = \alpha_c(\hat{R_f} + R_a) \tag{3.25}$$

Replacing the term R_a with its definition from equation (3.23) gives

$$Kp_c = \alpha_c \hat{L_f};\ Ki_c = \alpha_c(\hat{R_f} + \alpha_c \hat{L_f} - \hat{R_f}) \tag{3.26}$$

which results in the calculation of the improved PI controller parameters as

$$Kp_c = \alpha_c \hat{L_f};\ Ki_c = \alpha_c^2\, \hat{L_f} \tag{3.27}$$

Now it is clear why the above-derived controller may be referred to as having two degrees of freedom: it uses two inputs, the error signal $\underline{e}$ and the current $\underline{i}_f(t)$ directly via the active damping term [21].

3.4.3 Analysis of the current controller

In order to make a detailed analysis of the controller, it is necessary to derive the transfer function from the current $\underline{\mathrm{i}}_f(s)$ to the reference $\underline{\mathrm{i}}_{f,ref}(s)$ to obtain the poles and zeros of the function. Making the assumption that with the feed-forward terms in the controller the system is linearized and decoupled and that the parameter estimation is perfect, the two sides of the control signal $\underline{v}_c'(s)$, as seen in Figure 3.6, are studied:

$$\underline{v}_c'(s) = (sL_f + R_f + j\omega L_f)\underline{i}_f(s) + \underline{e}_g(s) \tag{3.28}$$

$$\underline{v}_c'(s) = \Big(Kp_c + \frac{Ki_c}{s}\Big)[\underline{i}_{f,ref}(s) - \underline{i}_f(s)] + (j\omega \hat{L_f} - R_a)\underline{i}_f(s) + \underline{e}_g(s) \tag{3.29}$$

Similarly to what is done in the previous section, equating both expressions as $\underline{v}_c'(s) = \underline{v}_c'(s)$ and developing gives

$$(sL_f + R_f)\underline{i}_f(s) = \Big(Kp_c + \frac{Ki_c}{s}\Big)[\underline{i}_{f,ref}(s) - \underline{i}_f(s)] - R_a\underline{i}_f(s) \tag{3.30}$$

arranging the elements returns

$$\underline{i}_f(s)(s^2L_f + s(R_f + R_a + Kp_c) + Ki_c) = (sKp_c + Ki_c)\underline{i}_{f,ref}(s) \tag{3.31}$$

from which finally the transfer function to be analyzed is

$$\frac{\underline{i}_f(s)}{\underline{i}_{f,ref}(s)} = \frac{(sKp_c + Ki_c)}{s^2L_f + s(R_f + R_a + Kp_c) + Ki_c} \tag{3.32}$$

Considering the definition of the controller gains and the active damping, as previously defined from equations (3.23) and (3.27) and substituting them into equation (3.32) yields

$$\frac{\underline{i}_f(s)}{\underline{i}_{f,ref}(s)} = \frac{\alpha_c\Big(s + \frac{\hat{R_f}+R_a}{\hat{L_f}}\Big)}{(s+\alpha_c)\Big(s + \frac{\hat{R_f}+R_a}{\hat{L_f}}\Big)} \tag{3.33}$$

where the tilde "hat" indicates that the parameters are now the estimated ones.

Looking at equation (3.33), it becomes apparent that the zero is cancelled out by one of the poles and that the close-loop current controller is a first-order transfer function.

3.5 Voltage limiter

When deriving the controller, the system is treated as ideal. However in practice this is not the case. The terminal voltage of the converter, for example, cannot be made arbitrarily large. It has to be restricted to the converters physical limits. This is the reason why a saturation is implemented at the output of the current controller to limit the voltage magnitude to the maximum voltage the converter can produce. The angle is kept the same since it is the angle that governs the power transfer.

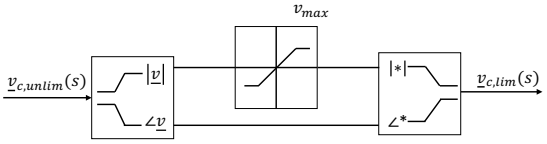

Figure 3.7: Voltage limiter implementation at the output of the current controller

3.6 Reference calculation

In $\alpha\beta$, the instantaneous active and reactive power can be calculated respectively as

$$p(t) = \frac{3}{2K^2}\Big(v_\alpha(t)i_\alpha(t) + v_\beta(t)i_\beta(t)\Big) \tag{3.34}$$

$$= \frac{3}{2K^2}\Re\Big\{\underline{v}^{\alpha\beta}(t)\,\underline{i}^{*\alpha\beta}(t)\Big\} \tag{3.35}$$

and

$$q(t) = \frac{3}{2K^2}\Big(v_\beta(t)i_\alpha(t) + v_\alpha(t)i_\beta(t)\Big) \tag{3.36}$$

$$= \frac{3}{2K^2}\Im\Big\{\underline{v}^{\alpha\beta}(t)\,\underline{i}^{*\alpha\beta}(t)\Big\} \tag{3.37}$$

where K is an arbitrary scaling constant, which is selected as $\sqrt{\frac{3}{2}}$ in order to achieve a power-invariant scaling

$$K = \sqrt{\frac{3}{2}} \Rightarrow p(t) = u_\alpha i_\alpha + u_\beta i_\beta \tag{3.38}$$

Considering that the formula for the complex power $\underline{S}(t)$ is

$$\underline{S}(t) = P(t) + jQ(t) = \left(\underline{u}(t)\,\underline{i}^*(t)\right) \tag{3.39}$$

$$\underline{S}(t)^* = P(t) - jQ(t) = \left(\underline{u}^*(t)\,\underline{i}(t)\right) \tag{3.40}$$

Then, aligning the grid voltage vector on the d-axis gives $u(t) = u_d(t)$, the reference for the d component of the current becomes

$$i_{d,ref,unlim}(t) = \frac{P(t)}{u_d(t)} \tag{3.41}$$

and similarly for the q component

$$i_{q,ref,unlim}(t) = \frac{-Q(t)}{u_d(t)} \tag{3.42}$$

3.7 Implementation of a current limiter

Similarly to the voltage, a current limiter is implemented at the output of the reference calculation block. This is done to ensure that the set-point changer is limited to the actual physical ratings of the components of the system. Different limiting strategies exist, such as prioritizing one current component over the other or choosing to limit the magnitude but keeping the angle, as it was done in the voltage limiter. Since the aim is to provide frequency support and that the voltage support is a secondary service, the d_{ref} component will be given priority and the q_{ref} component will be limited to the remaining capacity of the inverter. The implementation is shown in Figure 3.8.

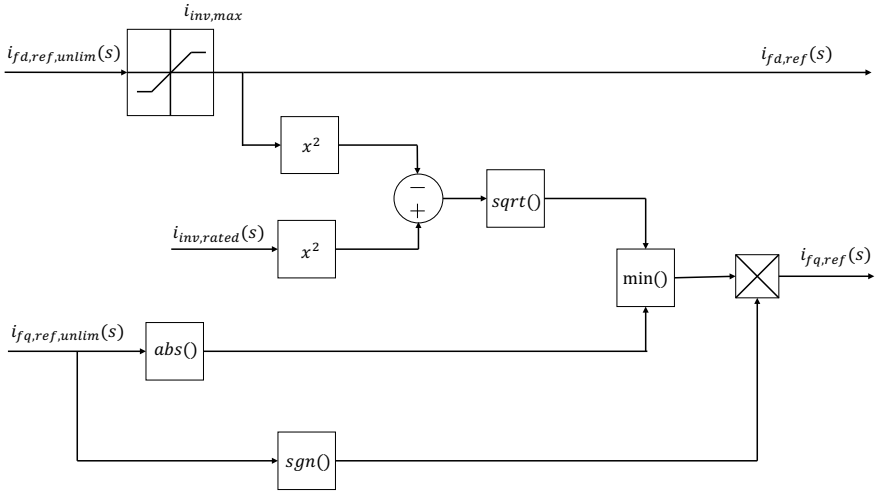

Figure 3.8: Current limiting strategy that prioritizes the d component and relegates the q component to the remaining capacity of the inverter

3.8 Derivation of anti-windup function for the integrator

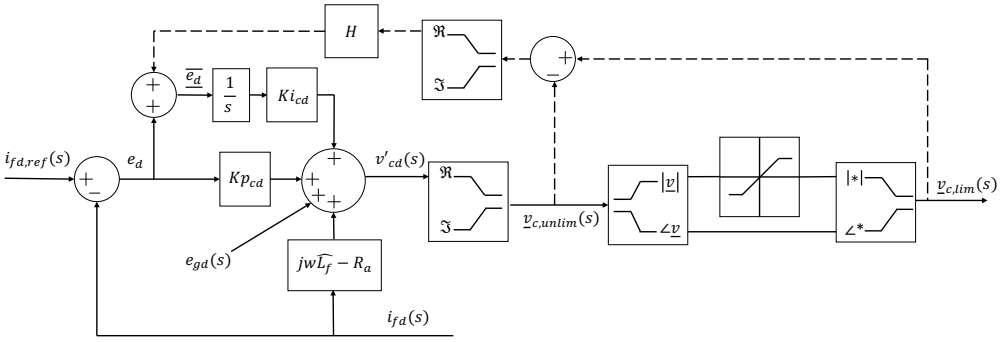

Figure 3.9: Depiction of an anti-windup function for the real component of the current controller. Dashed lines indicate back-calculation paths for the modified error signal of the integrator

The limitations imposed at the set-point changer have as a consequence that in case of large steps in the current, the integral part of the PI controller gets "overcharged" due to the limited response in $\underline{i}_{f,ref}(s)$. This occurs because the integrator keeps accumulating error, producing an overshoot in the response. This would continue to be the case until the windup is taken care of by a large negative control error [21]. A solution is to feed a modified error signal into the integrator in order to limit the integration when the output voltage of the current controller is limited.

Figure 3.9 shows the current control loop together with the implementation of a voltage saturation. The dashed lines indicate the signal paths to "back calculate" the error signal when the output voltage is $\underline{v}_{c,unlim}(s) > V_{max}$. The function H is a gain to act on the added feed-forwarded loop.

First, we examine the control signal $v'_{cd}(s)$

$$v'_{cd}(s) = \Big(Kp_{cd} + \frac{Ki_{cd}}{s}\Big)\Big(i_{fd,ref}(s) - i_{fd}(s)\Big) + (j\omega\hat{L_f} - R_a)i_{fd}(s) + e_{gd}(s) \quad (3.43)$$

We define the error signal e_d entering into the proportional part as

$$e_d = i_{fd,ref}(s) - i_{fd}(s) \quad (3.44)$$

and the error signal from the integrator, I_d as

$$I_d = \int e_d \, \mathrm{d}t = \int \Big(i_{fd,ref}(s) - i_{fd}(s)\Big) \, \mathrm{d}t \quad (3.45)$$

then, by inserting equations (3.44) and (3.45) in (3.43) we get

$$v_{cd}(s) = Kp_{cd}\, e_d + Ki_{cd}\, I_d + (j\omega L_f - R_a)i_{fd}(s) + e_{gd}(s) \quad (3.46)$$

We now define a new integrator error signal as

$$\underline{I}_d = \int \underline{\overline{e}}_d \, \mathrm{d}t \tag{3.47}$$

We then analyze the output $\underline{v}_{c,lim}(s)$

$$v_{cd,lim}(s) = Kp_{cd}\,\underline{\overline{e}}_d + Ki_{cd}\,\underline{I}_d + (j\omega L_f - R_a) i_{fd}(s) + e_{dg}(s) \tag{3.48}$$

Equating equations (3.46) and (3.48), and simplifying terms

$$v'_{cd}(s) = v_{cd,lim}(s) \tag{3.49}$$

$$v_{cd,lim}(s) - v'_{cd}(s) = Kp_{cd}\,\underline{\overline{e}}_d - Kp_{cd}\,e_d \tag{3.50}$$

It is now possible to define the modified integrator error $\underline{\overline{e}}$ as

$$\underline{\overline{e}}_d = e_d + \frac{1}{Kp_{cd}}\Big(v_{cd,lim}(s) - v_{cd}(s)\Big) \tag{3.51}$$

where it is evident that $1/Kp_{cd}$ is the value of the function H from Figure 3.9.

3.9 Outer controllers

3.9.1 Frequency controller

The goal is to reduce the rate-of-change-of-frequency, therefore a simple P controller is sufficient. K_{pf} is the proportional component that acts on the measured frequency deviation. Its value its chosen in $p.u.$ according to the maximum allowed frequency deviation. Figure 3.10 shows the proposed control. $f_{meas,pu}$ is the frequency measurement from the PLL in $p.u.$. $f_{ref,pu}$ is the reference frequency in $p.u.$

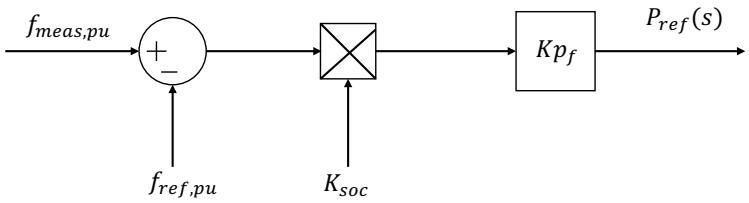

Figure 3.10: Block diagram of the frequency controller consisting of a proportional gain and a droop

K_{soc} is a droop factor introduced to take into account the limited battery capacity, thus as the battery SOC reaches a limit (maximum or minimum), the BESS equivalent frequency droop will be gradually reduced by means of K_{soc}. This droop characteristic will be further explained in Section 3.11.

3.9.2 AC voltage controller

The voltage controller is implemented as a single droop controller. Its implementation is shown in Figure 3.11a. The controller computes the difference between the magnitude of the voltage measurement from the grid and the reference.

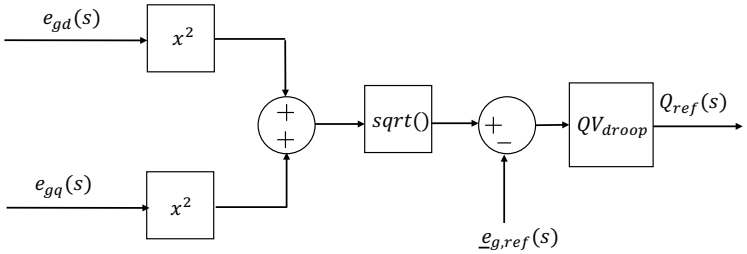

(a) Block diagram of the AC voltage controller

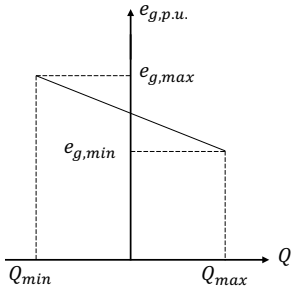

(b) Voltage droop slope for the voltage controller

Figure 3.11: Elements of the voltage AC outer controller

QV_{droop} is a general voltage droop representing the slope of the voltage as in Figure 3.11b.

3.10 Battery

Modelling batteries is the process of describing the phenomena that occur inside the battery through mathematical equations. Two main types of models exist: on one hand there are the electrochemical models that describe the reactions and physical processes taking place inside the battery. On the other hand, electric circuit-based models are useful to represent electrical characteristics of batteries [17].

The most simple electric model is shown in Figure 3.12, which consists only of a constant resistance R_b in series with an ideal voltage source E_0. This model, however, does not take into account the battery's internal dynamics and some of the element's non-linearities, which makes it only suitable for very simplistic modelling [22].

More accurate models for dynamic simulations, that can accurately represent the electrical behaviour of four distinct battery types: Lead-Acid, Li-Ion, NiMH and NiCd, alongside important internal states such as the SOC, are proposed in [23, 24].

In [23], the author describes a universal battery model intended for applications in dynamic simulations. It uses a non-linear equation to describe the voltage source's behaviour based on the SOC-level, which in turn is estimated by integrating the current. The non-linear voltage equation uses the electrochemical behaviour of a

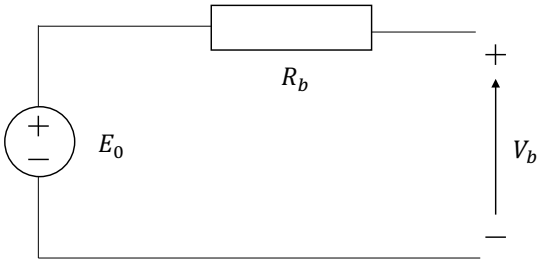

Figure 3.12: Simple battery model consisting only of a resistance in series with an ideal voltage source

battery in terms of terminal voltage, open circuit voltage, internal resistance, discharge current and SOC. A graphical representation of the model is presented in Figure 3.13.

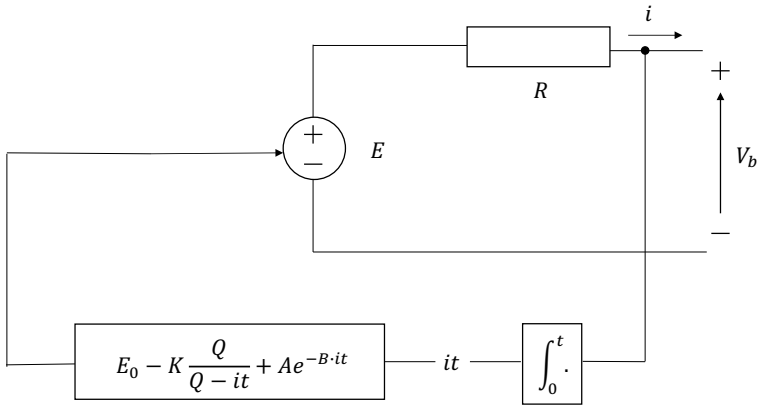

Figure 3.13: Dynamic battery model which uses a non-linear equation to control the voltage source

where
V_b = no-load voltage (V)
E_0 = battery constant voltage (V)
K = polarisation voltage (V)
Q = battery capacity (A h)
A = exponential zone amplitude (V)
B = exponential zone time constant inverse (A h^{-1})
R = internal resistance (Ω)
i = battery current (A)
$it = \int_0^t i\,\mathrm{d}t$ = integrated battery current (A h)

The exponential zone A represents the fully charged area comprised between the point of full charged voltage and the beginning of the nominal area. This is shown in Figure 3.14, which illustrates a typical nominal current discharge characteristic obtained using the model in [23], for a 3.5 V, 1 A h Li-Ion battery for a discharge

current of 10 A (10 C-rate).

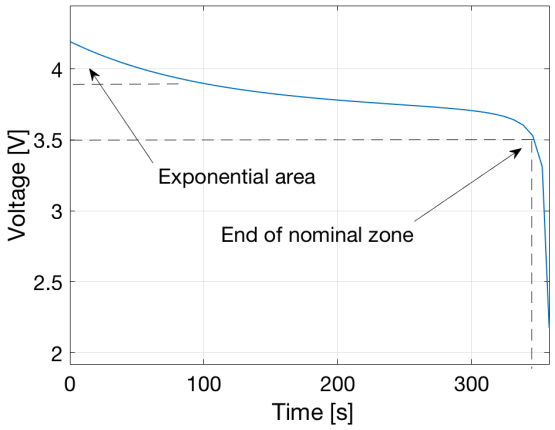

Figure 3.14: Typical discharge curve of a 3.5 V, 1 A h Li-Ion battery for a 10C discharge rate. $E_0 = 3.7348$, $K = 0.00876$, $Q = 1$, $A = 0.468$, $B = 3.5294$, $R = 0.09$.

According to the author, the model presented in [23] is valid in steady state (constant current) but this model produces false results when the current varies.

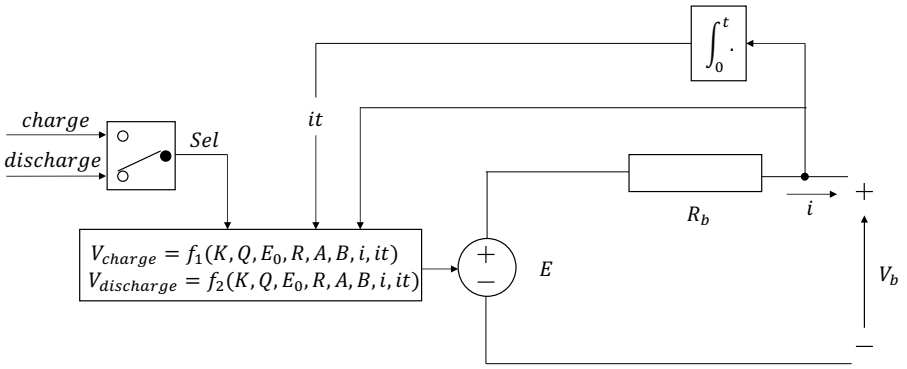

Figure 3.15: Diagram showing a dynamic battery model with charge and discharge capabilities. It uses a non-linear voltage source dependent on the current and the integrated current flowing trough the battery

On [24], the author presents an improved version of the dynamic battery model that can be applied both for discharge and charge dynamics. It uses the same electromechanical parameters as in [23] to represent the dynamic behavior of the voltage. In the particular case of [24], for a Li-Ion battery, the adapted non-linear voltage equation for the discharge phase is

$$V_b = E_0 - R \cdot i - K\frac{Q}{Q - it} \cdot (it + i) + Ae(-B \cdot it) \tag{3.52}$$

and for the charge phase

$$V_b = E_0 - R \cdot i - K\frac{Q}{it - 0.1 \cdot Q} \cdot i - K\frac{Q}{Q - it} \cdot it + Ae(-B \cdot it) \tag{3.53}$$

The layout of a dynamic battery model adapted from [24] is presented in Figure 3.15. It can be seen how the voltage source E_0 is controlled by non-linear equations that provide valid results for both charge and discharge dynamics.

3.11 Battery management system

The BMS, handles actions related to the battery's condition. In the proposed BESS ancillary service, it interacts with the system's first level of control by using the battery's SOC as input and providing the operational parameter K_{soc} which acts as a droop to limit the contribution of the system in order to protect the battery.

The proposed BMS scheme, based on [25], uses a power-curtailment strategy when the battery's SOC reaches critical levels. The curtailment mechanism provides a smooth transition between the normal operation and idle operating points. Thus, by allowing the battery to gradually reduce its output, a sudden loss of support power is prevented therefore preventing further disturbance to the grid [25].

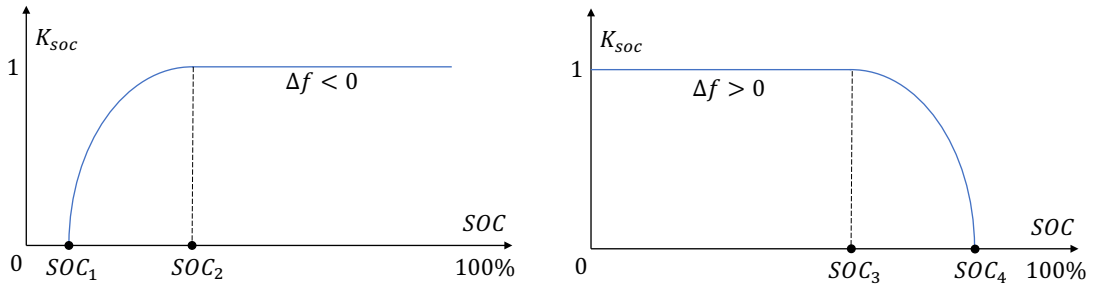

(a) Evolution of K_{soc} when the frequency deviation Δf is negative. SOC_1 indicates an idle point of operation and SOC_2 represents the point at which the droop limits the BESS compensation

(b) Evolution of K_{soc} when the frequency deviation Δf is positive. SOC_3 illustrates the point at which the droop starts to act in order to limit the BESS compensation and SOC_4 represents the idle operation point

Figure 3.16: K_{soc} droop characteristics

Figure 3.16 shows how the droop component K_{soc} depends on the frequency deviation Δf. When load exceeds generation, or when a generating unit is lost, a frequency dip ensues and thus $\Delta f < 0$. In that case, the droop will act as depicted in Figure 3.16a. It is clear the battery's compensation level will begin to decrease at the point SOC_2 until the point SOC_1 when the battery stops injecting power

completely, in order to avoid a total discharge of the battery cells.

Conversely, when there is excess power in the system, Δf will be positive. In such an instance, the droop component will behave as illustrated in Figure 3.16b. There, the BMS begins restricting the battery compensation when the SOC reaches the operation point SOC_3, and the battery stops charging completely at the operation point SOC_4. The operational points (*e.g.* $SOC_1 = 5\%, SOC_2 = 15\%, SOC_3 = 80\%$ and $SOC_4 = 90\%$ of SOC) depend on the battery's physical constraints, as well as on the preferred support strategy.

For example, if the BESS is intended exclusively to mitigate frequency dips, then the values for SOC_3 and SOC_4 can both be set to 100%, so that there is no droop component when the battery is charging. This in order to maximize the availability of the battery's capacity. On the other hand, if the BESS is intended to mitigate both negative and positive frequency regulations, it is important to restrict the maximum battery charging to a certain level in order to have capacity available to absorb power if needed.

4

Implementation and model verification

This chapter presents the reader with the implementation approach and validation of the derived models in the simulation tool PowerFactory.

4.1 Implementation approach

The implementation of this thesis was carried out using DIgSILENT GmbH PowerFactory® 2016 SP3 Build 16.0.4(6018)/Rev. 36850. PowerFactory is an engineering simulation software developed for the analysis of transmission, distribution and industrial electrical power systems. It can be applied as a simulation tool for, to name a few: load flow analysis, short-circuit analysis, power quality and harmonic analysis, quasi-dynamic as well as dynamic simulations, contingency analysis, eigenvalue analysis and many others [26].

The software is extremely capable and comes pre-loaded with many standard models like governors, power system stabilizers, etc. with different levels of detail. It is, however, also possible to implement user-defined models that can be interfaced alongside standard models and network elements [19].

For the dynamic simulations, all tests were conducted using the RMS simulation method.

4.1.1 RMS and EMT simulations

In PowerFactory, dynamic simulations can be performed using RMS (phasor-based) and EMT (electromagnetic transients) methods. In RMS simulations, electromagnetic dynamics of the electrical network are neglected and voltages and currents are defined as phasors. In this way, the voltages and currents in the network are found by algebraic equations rather than by differential equations [19].

$$\underline{v} = j\omega L\underline{i} \tag{4.1}$$
$$\underline{i} = j\omega C\underline{v} \tag{4.2}$$

The only differential equation considered in an RMS simulation is the swing equation for mechanical transients:

$$\frac{d}{dt}\frac{1}{2}J\omega^2 = P_{mech} - P_{el} \tag{4.3}$$

In EMT simulations, voltages and currents are represented by their instantaneous values, which means that the quantities are found by differential equations.

$$v = L\frac{d}{dt}i \tag{4.4}$$

$$i = C\frac{d}{dt}u \tag{4.5}$$

A disadvantage of EMT over RMS simulations is the very small simulation time-step needed to get accurate results. This makes simulations computationally-intensive and time-consuming, since the software engine has to solve a set of differential equations for a greater number of time-points. For transient stability studies as well as for evaluation of control systems, RMS simulation is preferable since the simplified network using phasors provides accurate enough results and allows for shorter calculation times. An in-depth comparison of RMS *versus* EMT results is discussed in detail in [19], where the authors conducted extensive testing and comparison of both simulation methods applied to slow dynamic studies of systems incorporating HVDC links.

4.1.2 Model revision

Taking the RMS simulation approach into consideration, the derivation of some parts of the control system have to be adapted. For the current controller, the term sL_f is neglected and thus, the system transfer function from equation (3.7) becomes

$$G_c(s) = \frac{\underline{i}_f(s)}{\underline{v}_c(s) - \underline{e}_g(s)} = \frac{1}{R_f + j\omega L_f} \tag{4.6}$$

which means that the one-degree-of-freedom controller parameters, as defined in equation (3.17), are now calculated as

$$Kp_c = 0;\ Ki_c = \alpha_c \hat{R}_f \tag{4.7}$$

Similarly, the active damping definition in equation (3.23) is modified to

$$R_a = \alpha_c - \hat{R}_f \tag{4.8}$$

and so, the two-degree-of-freedom controller parameters are

$$Kp_c = 0 \tag{4.9}$$

$$Ki_c = \alpha_c(\hat{R}_f + Ra) = \alpha_c(\hat{R}_f + \alpha_c - \hat{R}_f) = \alpha_c^2 \tag{4.10}$$

Finally, since $Kp_c = 0$, the definition of the anti-windup function, as obtained in equation (3.51), is now derived as

$$H = \frac{1}{\hat{R}_f} \tag{4.11}$$

4.1.3 Model evaluation

A simple arrangement consisting of the static generator and a controllable AC voltage source was implemented as the test grid. In this way, the behaviour of the control system can be evaluated by setting values for both frequency and voltage independently. Figure 4.1 shows the implementation of the simple test grid used to verify the models.

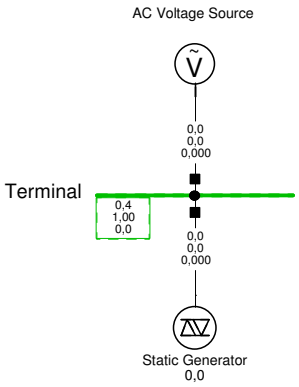

Figure 4.1: Single-line diagram of a simple test grid consisting of a controllable AC voltage source and a static generator representing the BESS

The battery system is represented in the network as a static generator, which is a model that can represent any kind of non-rotating generation unit. These types of generators include photovoltaic generators, storage devices, HVDC terminals, reactive power compensators, wind generators, etc. Basically any type of generation interfaced with the grid through a full-size converter can be modelled as a static generator, since the behaviour of the plant (as seen from the grid) is determined by the converter [27].

The static generator in PowerFactory supports four different models: voltage source, current source, constant impedance and constant power. It was decided to framework the system as a voltage source. The final expression of the voltage output from the current controller is expressed in equation (3.43), which is valid for both components dq.

It could be argued that static generator could also be modelled as a current source. However, in PowerFactory the current source model uses a built-in current controller defined in Figure 4.2. As stated before, in order for the RMS model to have the same response as the EMT model, the proportional part K, as seen in Figure 4.2, has to be set to 0. This makes the use of the built-in current controller only suitable for EMT simulations. Other reasons to implement a user-defined current controller using a voltage source model is that the built-in one is very basic and lacks a decoupling term, feed-forward of the grid voltage, active damping and it has no anti-windup function for the integrator.

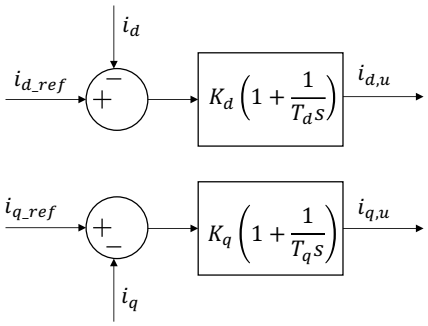

Figure 4.2: Built-in current controller for the static generator (DIgSILENT, 2016)

4.2 VSC control

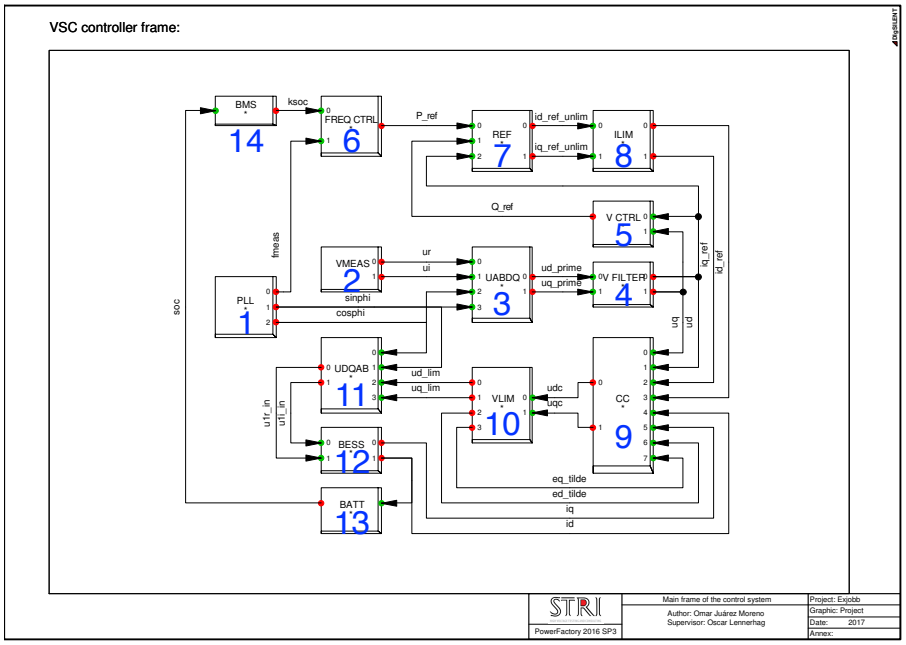

Figure 4.3: PowerFactory implementation of the control system of the Battery-based proposed ancillary service

Figure 4.3 illustrates the implementation of the proposed control strategy for the BESS in PowerFactory. A description of the blocks is provided in the following list:

1. The PLL input signals are the real and imaginary components of the voltage, which are automatically retrieved from the specified connection point. It outputs the signals *sinphi* and *cosphi* that together provide the phase angle information necessary for the *dq* transformations.

2. The VMEAS slot houses the voltage measurement. Just as the PLL, the input signals are connected automatically from the point of connection in the network. It outputs the signals ur and ui, which are the $\alpha\beta$ components of the measured grid voltage.

3. The UABDQ slot is the $\alpha\beta$ to dq transformation of the voltage signals ur and ui. It receives the information about the phase angle from the PLL slot.

4. The output voltage signals ud_prime and uq_prime are filtered in order to remove high frequency harmonic components that may affect the performance of the controller. Based on [25], the signals are passed through two Butterworth LPF with the function specified in equation (4.12), where the cut-off frequency ω_{cf} is chosen to be 100 times lower than the base switching frequency of the converter.

$$LPF(s) = \frac{\omega_{cf}^2}{s^2 + \sqrt{2}\,\omega_{cf} \cdot s + \omega_{cf}^2} \tag{4.12}$$

5. The Voltage controller receives the filtered voltage signals in dq as inputs and outputs the reactive power reference Q_{ref}.

6. The frequency controller inputs are the measured frequency $fmeas$ from the PLL and the K_{soc} droop component from the BMS.

7. The reference calculation block outputs the unlimited d and q current references which it calculates with the inputs from the outer frequency and voltage controllers, together with the filtered d component of the voltage.

8. The unlimited current references are capped in the ILIM slot, where the d component is given priority over the q one.

9. The current controller slot calculates the unlimited voltage control signals in dq.

10. The voltage limiter block restricts the magnitude of the output control voltage and outputs back the signals ed_tilde and eq_tilde, which are used for the back calculation of the integrator error for the anti-windup function implemented in the current controller.

11. The limited voltage control signal is rotated to the $\alpha\beta$ reference frame wit the block UDQAB.

12. The BESS model is interfaced with a static generator in the network. It receives the $\alpha\beta$ voltage control signals $u1r\_in$ and $u1i\_in$ and outputs the device current components in dq.

13. The battery block takes the measured current as input in order to compute the state of charge SOC.

14. The BMS takes in the SOC information from the battery to output the K_{soc} droop that will curtail the systems response capability in accordance to the battery's internal states.

4.3 Current controller

4.3.1 Basic current controller

The implementation of a basic current controller with only the decoupling feed-forward loop is presented in Figure 4.4. The parameters for the filter resistance and inductance are chosen respectively as 0.0025 and 0.25 in *p.u.* of the converter rated power.

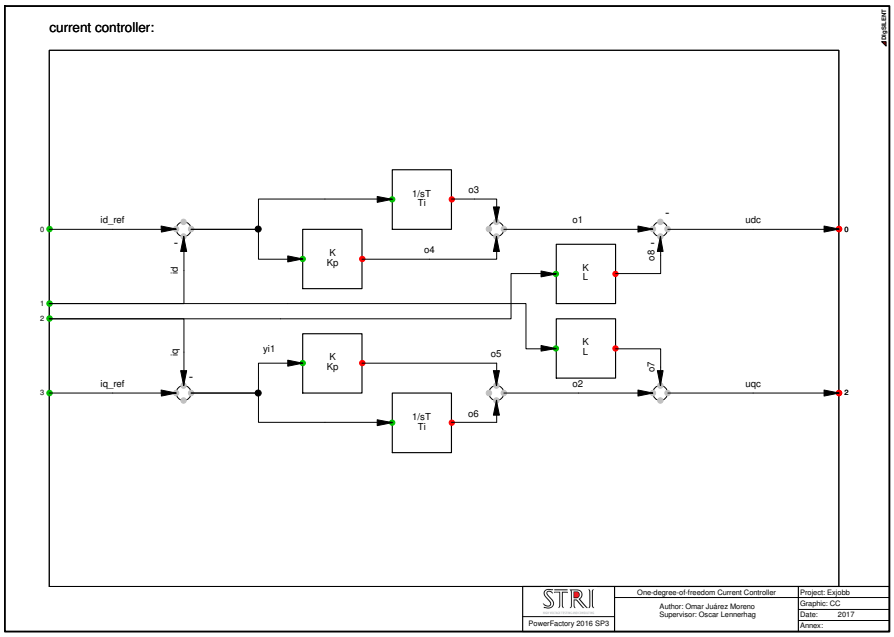

Figure 4.4: PowerFactory implementation of a one-degree-of-freedom current controller with decoupling term

In order to test the performance of the current controller, a 1 *p.u.* step in the d current is applied at 500 ms, as shown in Figure 4.5. The systems response to the step has the shape of a first-order system, as it was designed to do. The controller bandwidth α_c is chosen to be one tenth of the switching frequency of the converter, as suggested in [28]. The data points in the figure show the rise-time from 10% to 90% of the final value. As defined by equation (3.11), the data points evidence that the controller's bandwidth is 4 *p.u.*, which means that the controller is behaving as expected.

Figure 4.6 shows the response of the currents to a 0.5 *p.u.* step in the d current at 550 ms and a negative step with the same magnitude at 555 ms. The d component

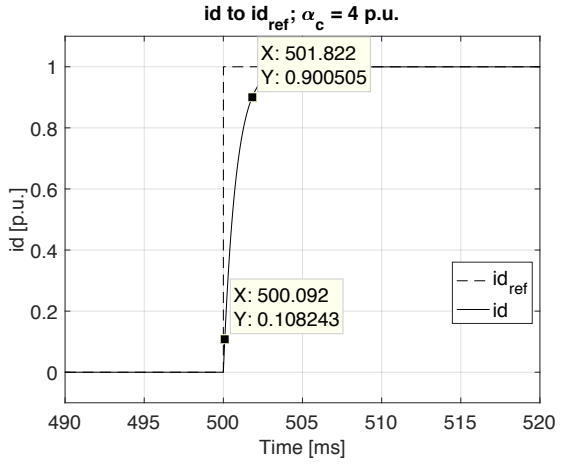

Figure 4.5: Basic current controller response after a 1 *p.u.* step in the *d* current is applied at 500 ms

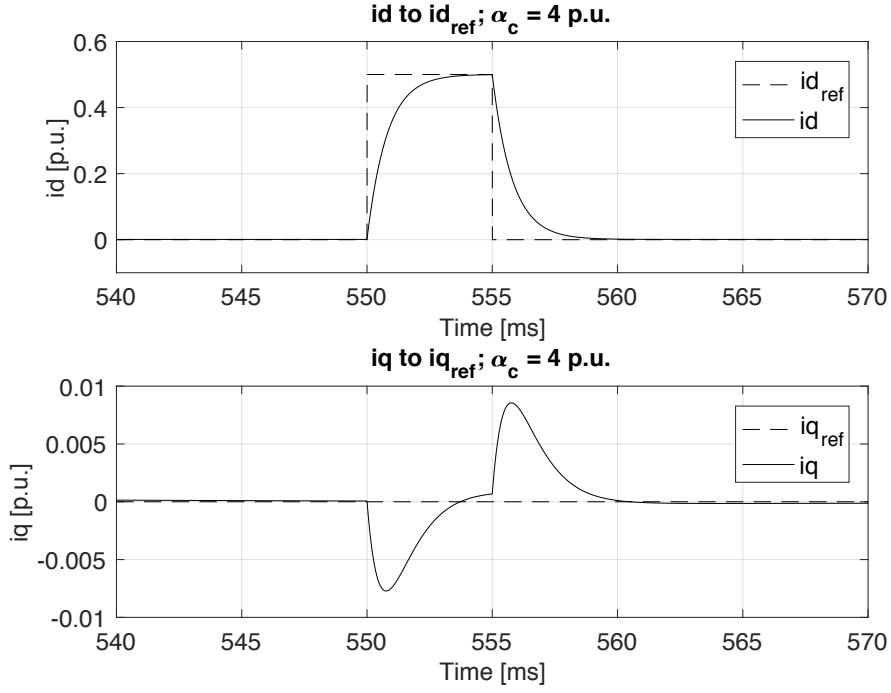

Figure 4.6: Controller currents response to set-point changes in the basic current controller from Figure 4.4 with decoupling term only

displayed in the top plot is behaving correctly. However, the q component exhibits disturbances in response to the set-point changes in the d component. The disturbances are small and quickly die out thanks to the action of the decoupling-term.

4.3.2 Improved current controller

Figure 4.7 displays the feed-forward of the grid voltage, active-damping and an integrator anti-windup function to the basic current controller.

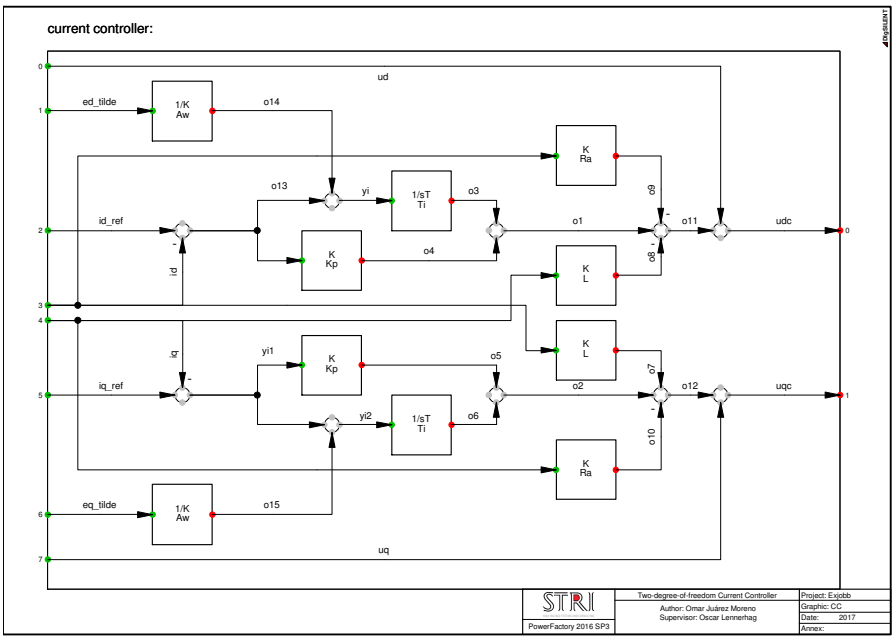

Figure 4.7: PowerFactory implementation of an improved current controller with feed-forward of the grid voltage, decoupling term, active-damping and an integrator anti-windup function

In order to corroborate that adding all these terms has not affected the behaviour of the system, a 1 $p.u.$ step in the d current is applied at 500 ms and its response (green) is superposed to the response from the basic current controller (dotted-black) in Figure 4.8. References are represented by the dashed-black lines. By looking at the shape of the response, it is evident that the controller continues to behave as expected and that the addition of the active damping term R_a has not affected the response's rise-time.

Figure 4.9 illustrates behaviour of the currents against set-point changes. The response of the improved current controller is shown in green and that of the basic current controller is the dotted-black line. References are the dashed-black lines. It is clear that the addition of active damping has a big effect on the robustness of the controller. This is specially evident when looking at the response of the q current after set-point changes in the d component. As opposed to the case without active damping, the disturbances in the q current are now completely damped, which

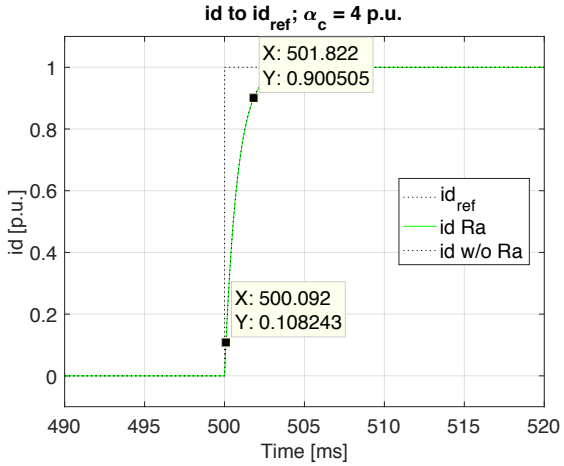

Figure 4.8: Current controller with added active damping response compared to a basic current controller after a 1 *p.u.* step in the d current is applied at 500 ms

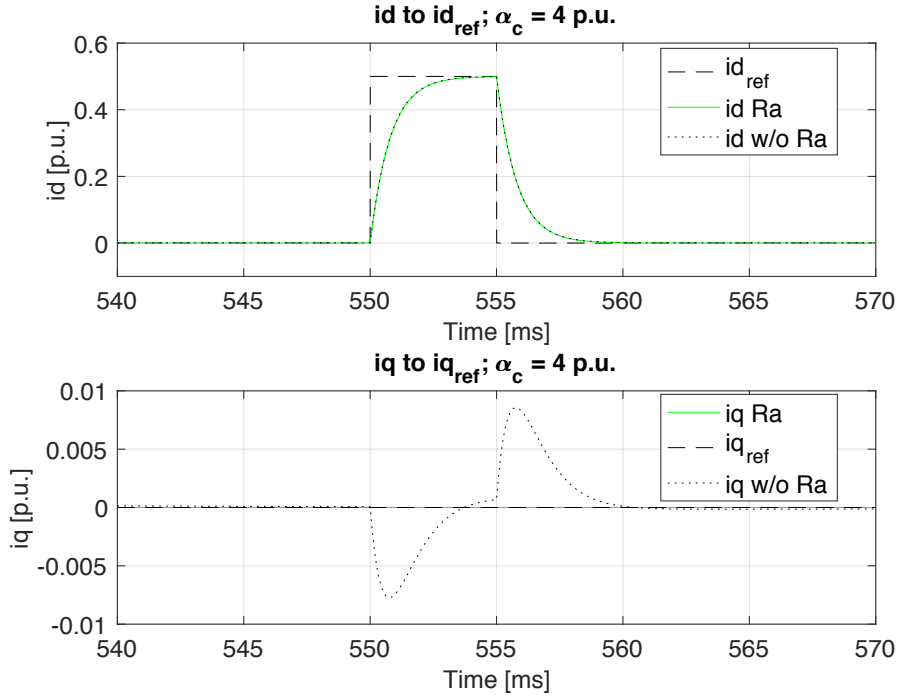

Figure 4.9: Comparison of the currents response to set-point changes between a basic current controller and an improved current controller with active damping

proves that adding active damping enhances the disturbance-rejection capability of the controller.

4.3.3 Current controller analysis

Figure 4.10 shows the results of the current controller transfer function analysis from $\underline{i}_f(s)$ to $\underline{i}_{f,ref}(s)$ at $\alpha_c = 4\,p.u.$. The plot in the upper left corner shows the pole-zero map of the controller without active damping. The controller pole (black) is positioned on the real axis at the controller bandwidth value 4 and the system pole (black) is positioned closer to the origin.

The lower left corner plot shows the position of the controller poles (green) with active damping. It is evident that with active damping, the system pole is moved to the controller pole, which gives a double pole at that position. This means that the controller with active damping is now insensitive to disturbances with bandwidth below 4 $p.u.$. The bode diagrams show the amplitude and phase margins for the controller without active damping (dotted-black) and with active damping (green). The fact that both curves are the same proves that adding active damping doesn't affect the frequency response of the controller.

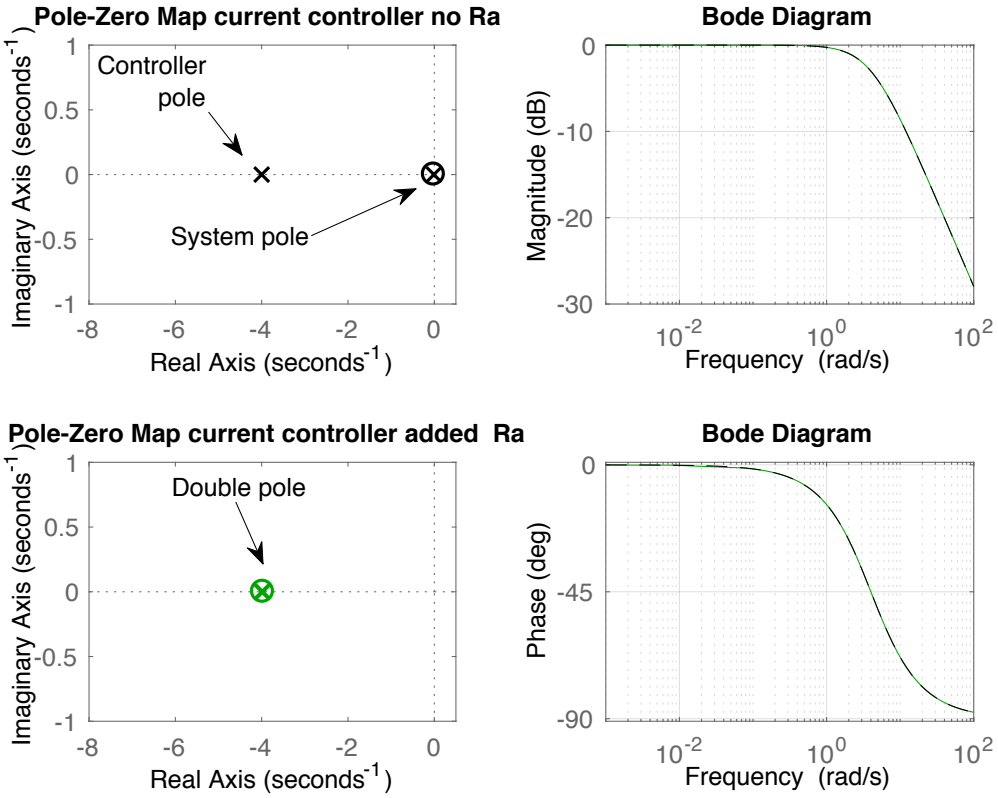

Figure 4.10: Analysis of the current controller with (green) and without (black) active damping. Pole placement is plotted in the complex plane and magnitude and phase margins in Bode plots. Note that the frequency axis units in Bode plots are in $p.u.$

4.3.4 Sensitivity to parameter variations

The parameters used to calculate the gains of the controller, $\hat{R_f}$ and $\hat{L_f}$ are the estimated values of the reactor filter R_f and L_f. In order to achieve good performance of the controller, the estimated values should be as close as possible to the actual values. However in practice, a perfect estimation is difficult to achieve. This is the reason why a parameter sensitivity analysis was conducted in order to study how the controllers behaviour is affected by imprecise parameter estimation.

4.3.4.1 Sensitivity to variations in the filter inductance

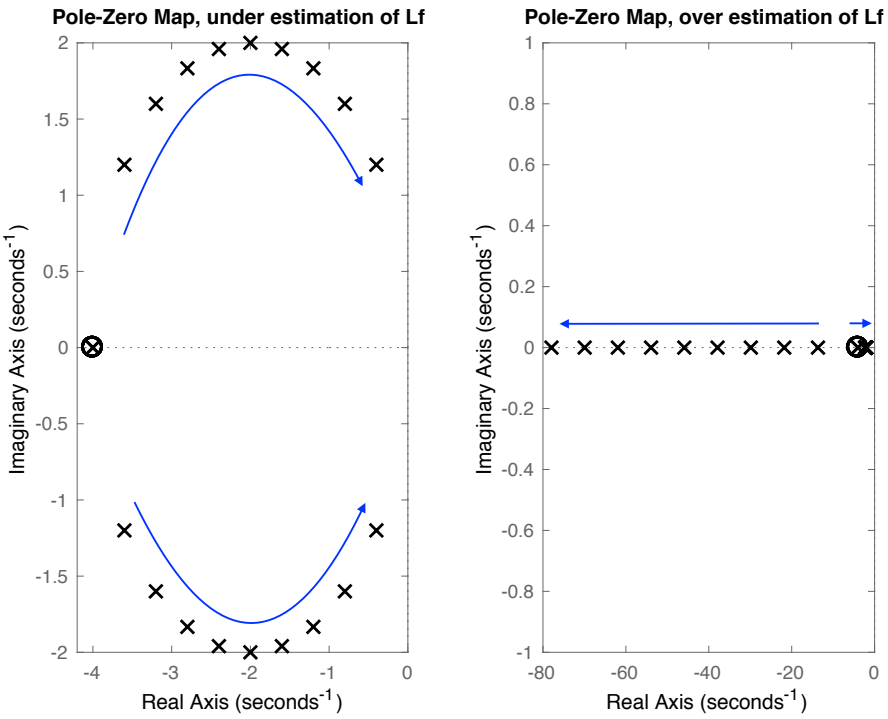

Figure 4.11: Pole-zero maps of the system's behaviour with an error in the estimation of the filter inductance $\hat{L_f}$

Figure 4.11 illustrates the pole placement in the complex plane for varying values of the filter inductance. The left hand plot shows the poles for an underestimation of L_f of the order $0.1L_f < \hat{L_f} < 1L_f$ in steps of 0.1. The right hand plot shows an overestimation of $L_f < \hat{L_f} < 10L_f$ in steps of 1. The non-zero imaginary parts of the solution in the left plot indicate an oscillatory behaviour. The left plot also shows that the smaller the inductance, the closer to the imaginary axis the poles move, approaching instability and making them more dominant. On the other hand, the right plot shows that overestimating the inductance has little effect on the system behaviour since it just pushes the poles away from the origin on the real axis.

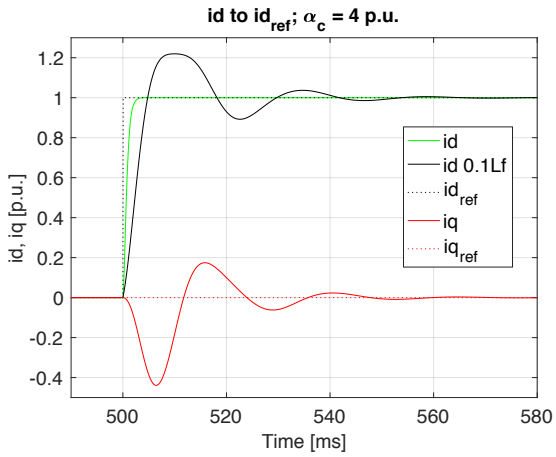

Figure 4.12: Oscillations in the current response to a unitary step and decoupling not working due to an under estimation of the estimated filter inductance $\hat{L_f} = 0.1L_f$

In order analyze the worst case (under estimation $\hat{L_f} = 0.1L_f$), a step of $p.u.$i n the d current was applied at 500 ms. The d component is plotted in solid black, the q in red, the references are dotted black and red, respectively and the systems response with perfect parameters is shown in green. As evidenced by the poles placement, the system has an oscillatory behaviour. Even though the controller has active damping, the q component is heavily affected by the step in the d current. This indicates that the decoupling is not working as expected. This comes as no surprise, since the decoupling term is the filter's reactance.

4.3.4.2 Sensitivity to variations in the filter resistance

Figure 4.13 shows the pole-zero maps for under and over estimation of the filter resistance $\hat{R_f}$. The left hand plot shows the behaviour of the system poles when the value is under estimated as $0.1R_f < \hat{R_f} < 1R_f$ in steps of 0.1. On the other hand, the right plot depicts the pole placement when $\hat{R_f}$ is varied as per $R_f < \hat{R_f} < 10R_f$ in steps of 1. Looking at the right hand plot of Figure 4.13, it is evident that over estimating the value of the filter resistance causes the system to respond in a slightly oscillatory manner. This is evidenced by the non-zero imaginary parts of the solutions that lean slightly towards the imaginary axis.

This response might seem counter-intuitive at first, since it is the resistive term that provides damping to the response of the controller, so one would expect that more resistance would mean a more damped system. However, a larger resistive term is translated into a slower rise time, so the integrating part computes a larger error and this gives as a result a larger integrator contribution and consequently an over shoot. This response is illustrated in Figure 4.14, where a step of $1\,p.u.$ was applied to the d component at 500 ms. The estimated resistive term is 10 times the value of the actual. The plot shows a small overshoot of $0.00015\,p.u$ in the d current response.

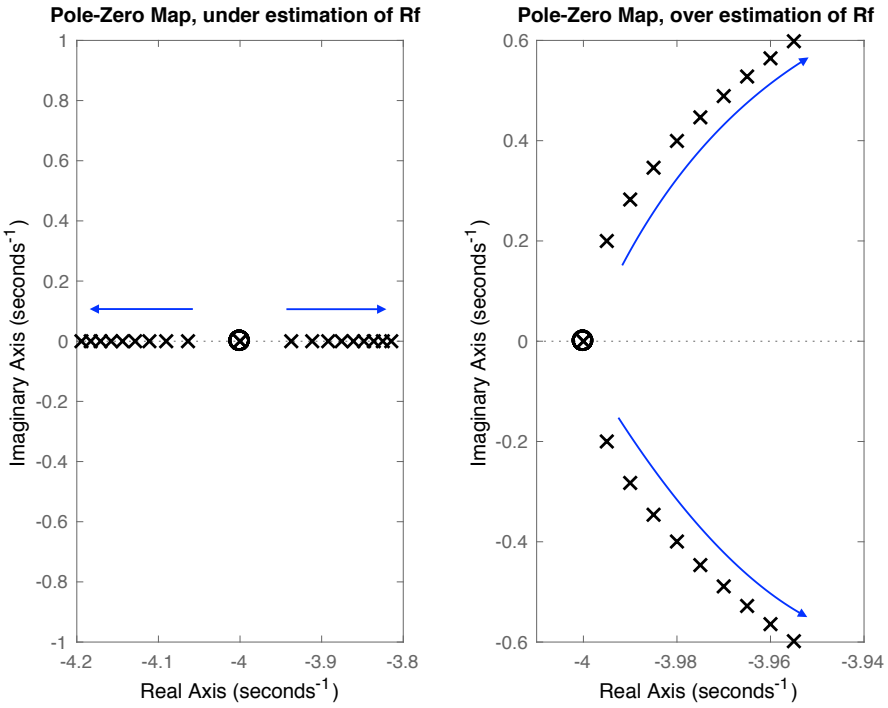

Figure 4.13: Pole-zero maps of the system's behaviour with an error in the estimation of the filter inductance $\hat{R}_f$

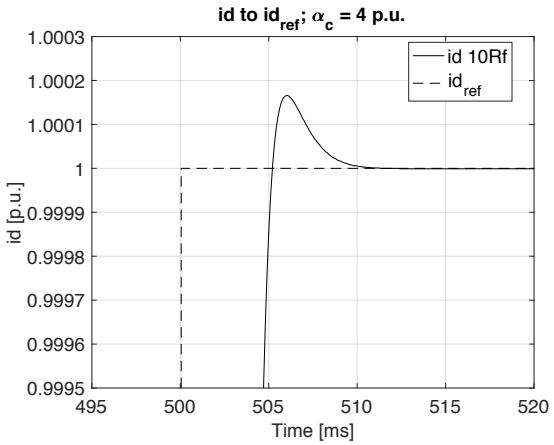

Figure 4.14: Overshoot in the d current response due to an over estimation of the filter resistance $\hat{R}_f = 10R_f$

4.4 Frequency controller

The block diagram of the frequency controller is shown in Figure 4.15. The difference between the measured and nominal frequency is passed trough a LPF with a time constant of 0.5 s. This filter is intended to mitigate the variation of the frequency estimation due to the phase angle jump after the disturbance is measured by the PLL. The time constant is chosen small in order to not affect the controller's set-point following.

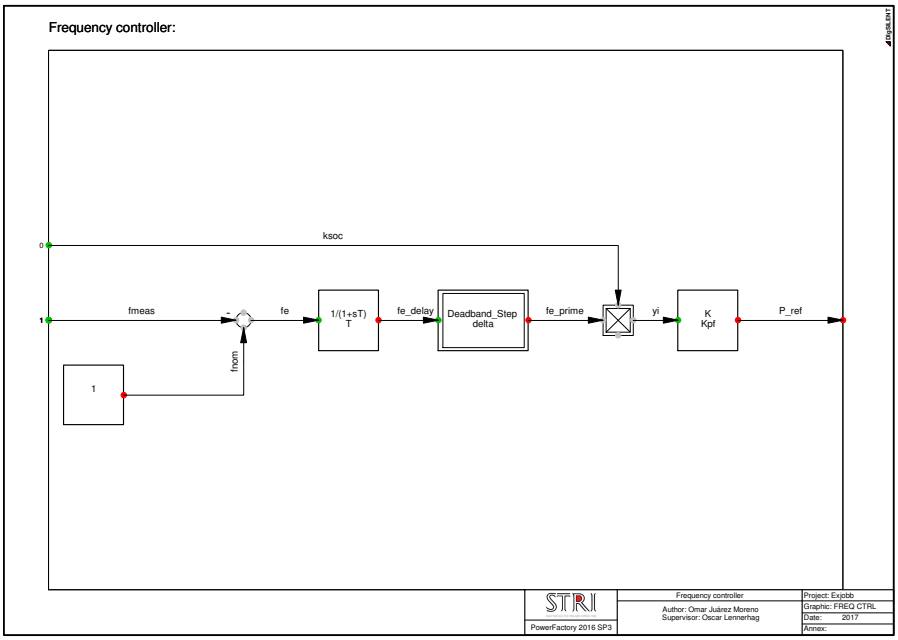

Figure 4.15: PowerFactory implementation of the outer frequency controller

The dead-band accounts for the fact that the proposed ancillary service is intended to provide FCR-D, which will only act on deviations outside the normal range of operations for the Nordic power system ($49.90 < f < 50.10$ Hz).

The resulting signal fe_prime is then multiplied with the droop K_{soc} coming from the BMS. The gain of the controller Kp_f is chosen in $p.u.$ according to the maximum allowed frequency deviation. In the case of FCR-D this value is 49.5 Hz (0.01 $p.u.$ for a nominal frequency of 50 Hz), So, for that case

$$Kp_f = \frac{1}{0.01} = 100 \tag{4.13}$$

where the numerator is the rating of the converter in $p.u.$ and the denominator is the maximum allow frequency deviation in $p.u.$ at which point the full BESS should be fully committed.

Figure 4.16 illustrates how the filter and the dead band work. Right after an event alters the frequency, the PLL phase-angle measurement experiences a step, which is registered in the calculated frequency coming into the controller. The signal fe is the difference between the calculated frequency signal from the PLL and the set-point nominal frequency $fnom$. In this case the event was at time 20s. However this signal entering the controller does not reflect the actual frequency deviation in the system, so the signal fe is filtered. The filtering action entails a delay, which is evident in the filtered signal fe_delay. The stepped dead-band then holds up the frequency controller action signal fe_prime until the frequency deviation is larger than $0.002\,p.u.$ in order to comply with FCR-D requirements.

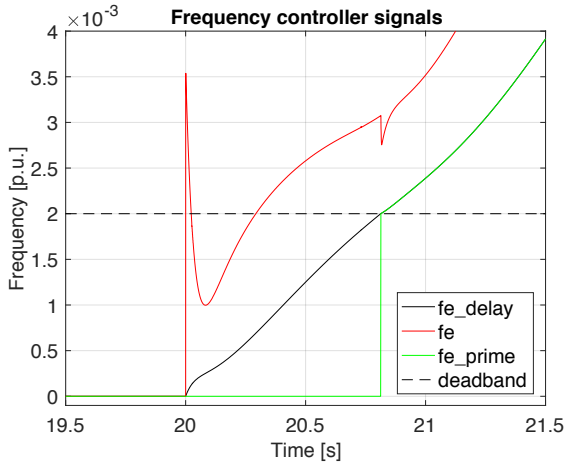

Figure 4.16: Frequency controller signals illustrating the effect of the filter acting on the frequency input and the dead-band

4.5 Current limiter

Figure 4.17 illustrates the principle of the current limiting strategy used, as explained in Section 3.7. On the right hand side plot, at time 470 ms, the controller is given a $0.1\,p.u.$ reference step in the q current, indicating that reactive power compensation is needed. At time 500 ms, the current controller receives a step in the d current of $1p.u.$, suggesting that there has been a big frequency dip and the whole converter capacity must be committed. Since the reference for the q current $(0.1\,p.u)$ is larger than the remaining converter capacity after the d current step $(1\,p.u.)$, the q component is curtailed.

On the left hand side plot, the current controller is given the same set-point changes, only that this time the d current reference is $0.9\,p.u.$. On this occasion, the converter is able to provide both active and reactive power compensation, so no curtailment on the q component is enforced.

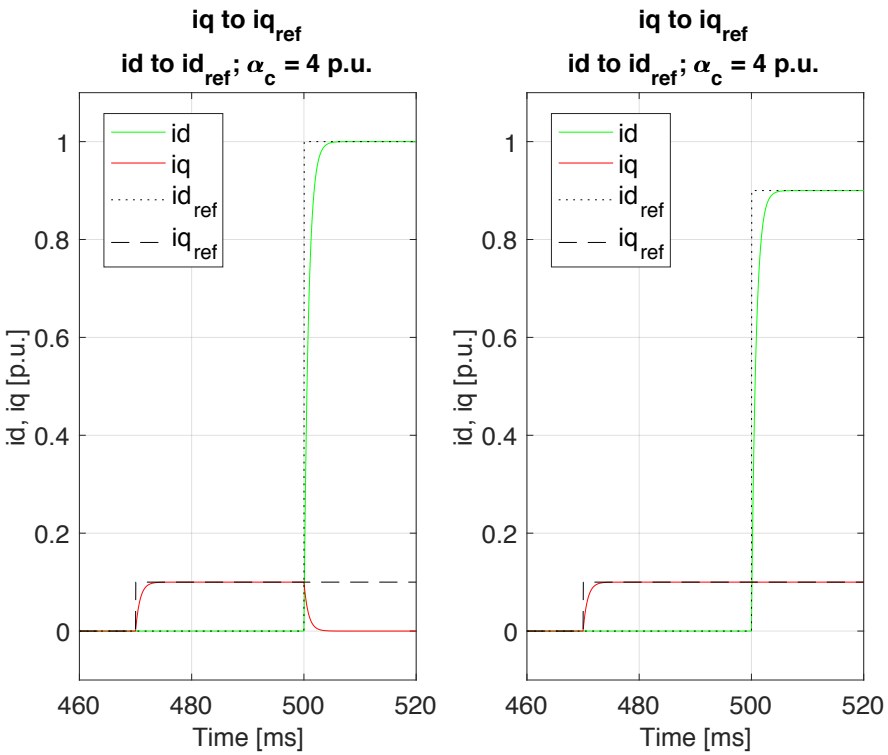

Figure 4.17: Current limiter giving preference to the d component of the current

4.6 Battery

The implementation shown in Figure 4.18 consists of two user-defined functions containing the charge and discharge equations defined in [24].

The discharge current of the battery can be adjusted using the scaling constant I_{bess}. The function selector works by comparing the magnitude of the current through the logic bloc "lower than". Once the adequate equation has been activated, it is feed the current and the integrated current, both of which pass through the inverted gain of the number of parallel cells, whose number decides the capacity of the battery. The output is the battery's voltage, which in turn is multiplied by the gain of the number of series cells to determine the battery's voltage level.

The battery's starting state of charge, SOC_{init}, can be set by adjusting the initial conditions of the integrator's state variable x with the equation

$$inc(x) = Q * n_{parallel} * \frac{SOC_{init}}{100} \tag{4.14}$$

Figure 4.19 shows the discharge curves for different C-rates. It demonstrates that the battery can deliver different levels of energy depending on the magnitude of the discharge current.

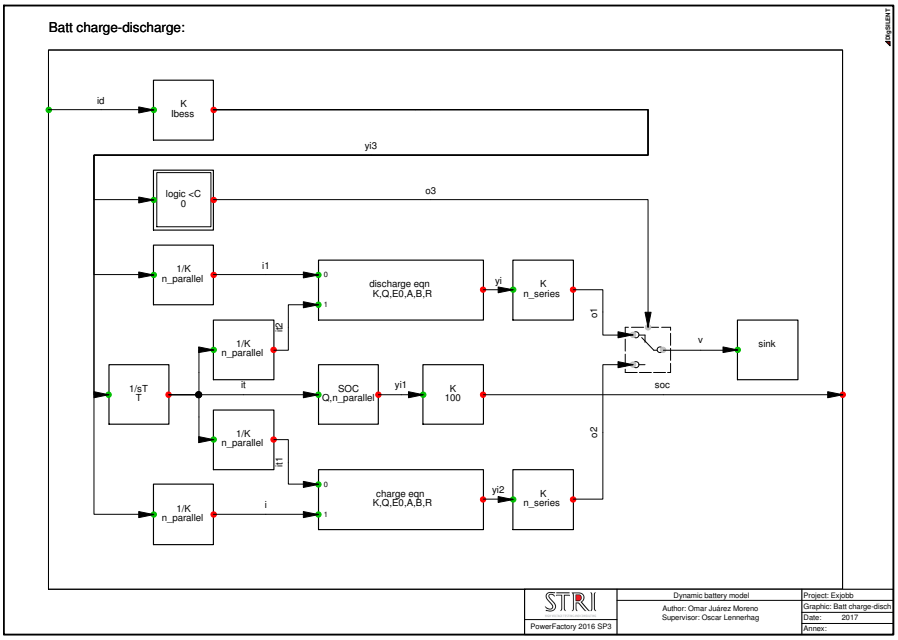

Figure 4.18: PowerFactory implementation of a dynamic battery model with charge/discharge capabilities

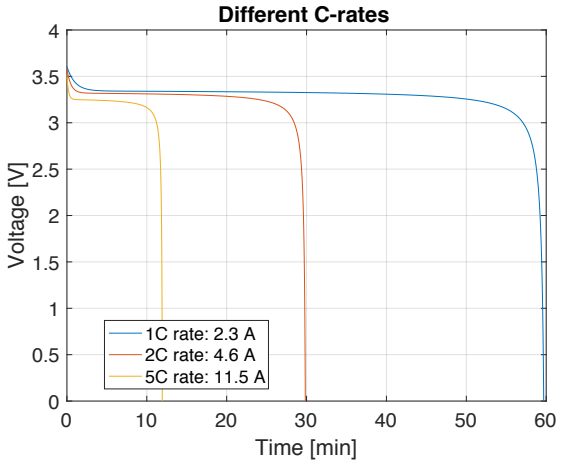

Figure 4.19: Nominal voltage discharge characteristic at different C rates for a 3.3 V, 2.3 A h Li-Ion battery.
$E_0 = 3.366, R = 0.01, K = 0.0076, A = 0.26422, B = 26.5487$

Figure 4.20 displays the dynamic behaviour of the battery's states when subjected to charge/discharge cycles. The battery voltage plot shows that at no load the battery's terminal voltage level is $E0$. It also illustrates that the terminal voltage is higher when charging than when discharging.

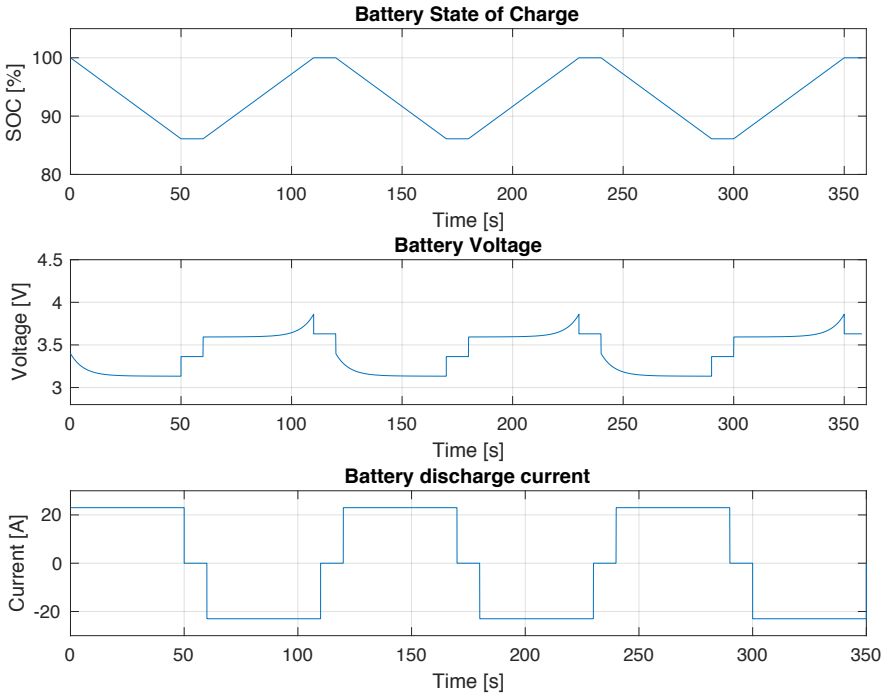

Figure 4.20: Battery's states of a 3.3 V, 2.3 A h Li-Ion battery when subjected to charge/discharge cycles.
$E_0 = 3.366, R = 0.01, K = 0.0076, A = 0.26422, B = 26.5487, C_{rate} = 10$

4.7 BMS

The SOC droop function is tested for the discharge logic only. Figure 4.21 depicts the different battery states when it is subjected to a complete discharge cycle. In this example, it is shown how the K_{soc} droop component begins to gradually reduce its level when the SOC reaches 25% and completely stops its output when the SOC reaches 5%, just before the end of the battery's nominal voltage area. It is evident that the K_{soc} droop, when connected to the frequency controller, would curtail the contribution of the BESS when the SOC is reaching low levels, thus preventing the battery from fully discharging and also avoiding a sudden loss of support power.

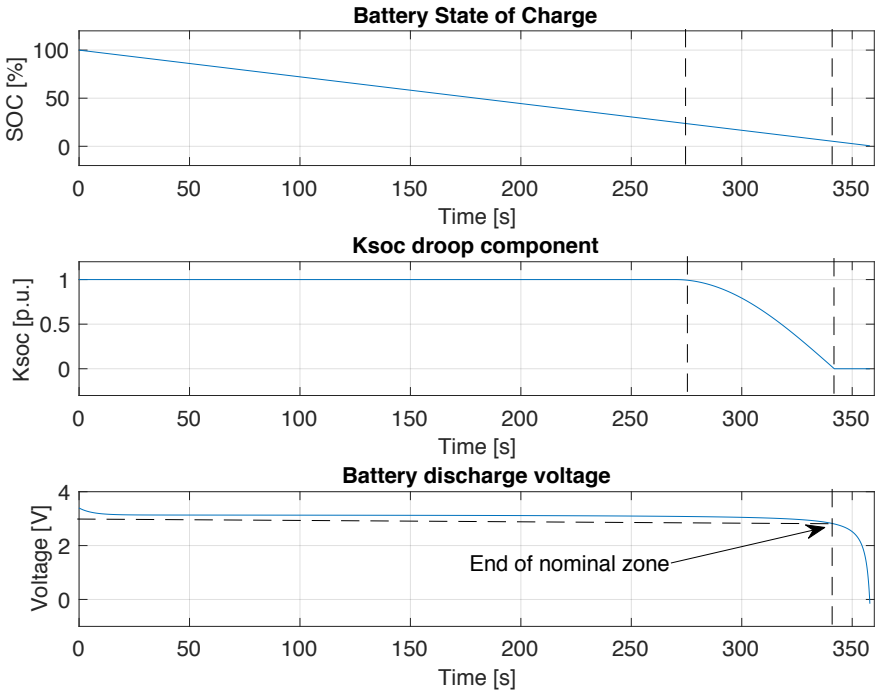

Figure 4.21: 3.3 V, 2.3 A h Li-Ion battery state of charge, K_{soc} droop component and nominal discharge curve.$E_0 = 3.366, R = 0.01, K = 0.0076, A = 0.26422, B = 26.5487, C_{rate} = 10$

5

Results from application study

This chapter's aim is to demonstrate the value of the proposed frequency-support ancillary service. It presents the results obtained from three study cases: the case of a single large frequency dip, a case with varying values of converter rating and the event of a partial replacement of thermal plants by wind farms in the Nordic32A bus system.

5.1 Test scenario

For the application study, the simulations were conducted in the Nordic32A system using the load-flow settings LF32_028. All the necessary information to replicate the system can be found on [7]. The implementation of the Nordic32A used in this thesis, together with the LF32_028 results obtained in PowerFactory, can be consulted in Appendix C. However, it is worth highlighting some dynamic data about the system, in addition to the information listed in Tables 5.1 and 5.2.

Table 5.1: System data from load flow LF32_028 (Svenska kraftnät, 1993)

Total generation	11 370 MW
Total load	10 940 MW
Total losses	430 MW

Table 5.2: Ratings and inertias (Svenska kraftnät, 1993)

Area	S_n (MVA)	$S_n \times H$ (MWs)
External	5000	15 000
North	6250	18 750
Central	3500	19 800
Southwest	1800	10 800
Total	16 550	64 350

The generators are represented by Park models including damper windings. Salient pole models are used for hydro generators (in addition to one asynchronous compensator), whereas thermal plants are modelled with round rotor generators. Only the hydro generating units are equipped with governors [7].

The load has the following characteristics:

- Voltage: Active power is assumed to linearly vary with voltage (constant current). Reactive power is assumed to have an impedance character.
- Frequency: Active power varies with frequency as follows: $P = P_0 \cdot (f/f_0)^{0.75}$.

The battery was dimensioned after the biggest battery storage system in the world [29] at the time of this writing: a 50 MW output and 300 MWh rated capacity BESS installed at the Buzen Substation in Buzen, Fukuoka Prefecture, Japan [30].

5.2 Frequency dip after 750 MW of generation is tripped

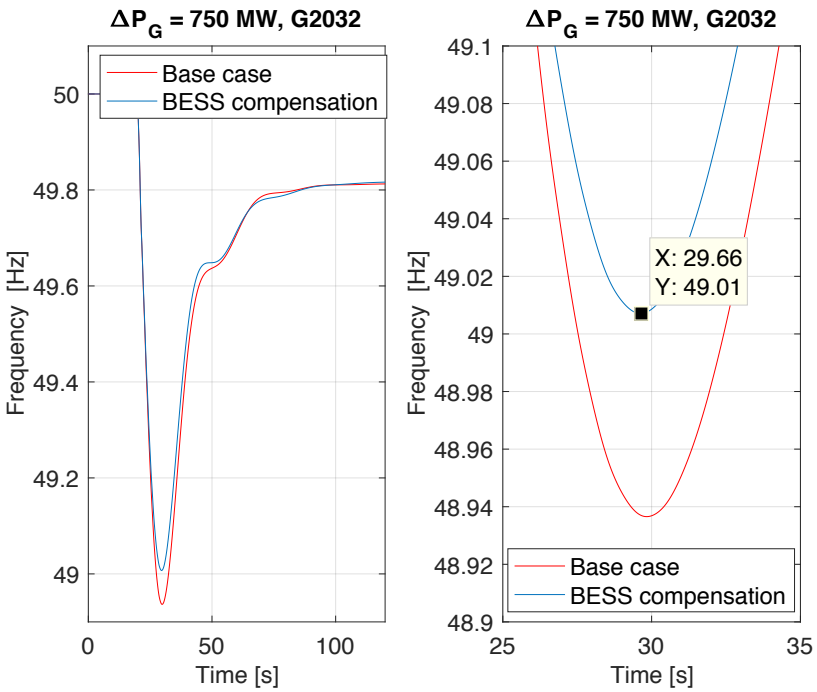

Figure 5.1: Frequency measurement showing the action of the BESS after 750 MW of generation is tripped. The right plot is a zoom of the frequency Nadir. 50 MW, 300 MWh BESS

The first case is a large frequency dip caused by the tripping of 750 MW of generation. In this case generator G2032 from zone North is disconnected at t =20 s. Figure 5.1 shows the frequency measurement of the base case in red and with BESS compensation in blue. It is evident that the action of the BESS prevented the frequency from going below 49 Hz. This action alone would have prevented more drastic frequency-control emergency actions such as load-shedding. It becomes clear that in this case the proposed ancillary service avoided disconnection of load and

affectations to costumers.

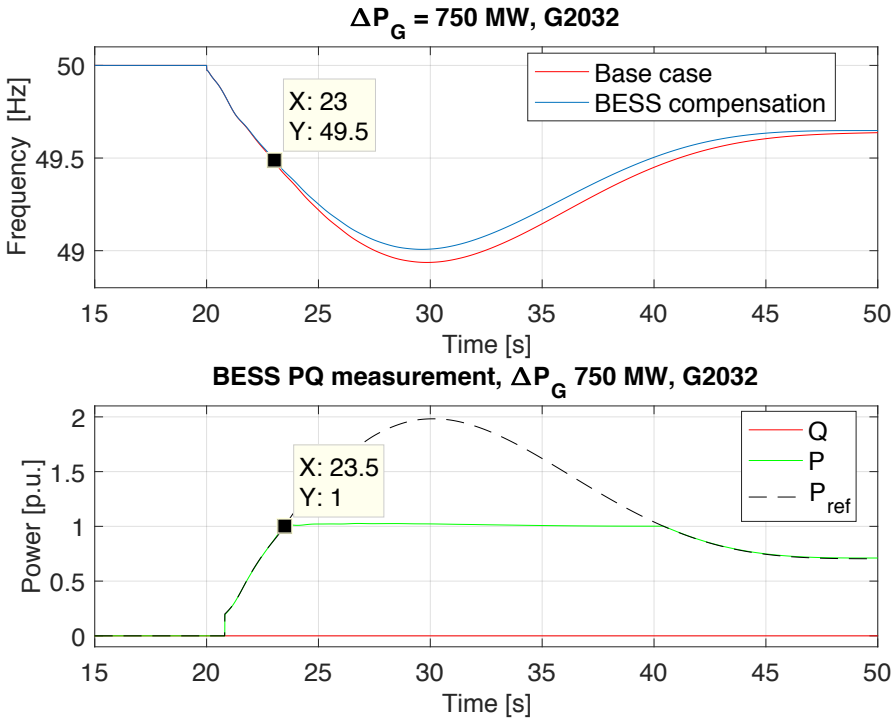

Figure 5.2: Frequency measurements for the base case and BESS compensated scenario after the loss of 750 MW of generation juxtaposed with the power measurements from the BESS. 50 MW, 300 MWh BESS

Figure 5.2 illustrates the frequency deviation above and the BESS power measurements below. There are a couple of interesting things to note. The data point on the upper plot indicates the time at which the frequency deviation reaches 49.5 Hz. It is clear that it is at 23 s. The data point on the lower plot marks the time instant at which the BESS is fully committed: at 23.5 s. The frequency controller was tuned so that the BESS could provide FCR-D, which indicates that the reserve should be fully committed at 49.5 Hz. Figure 5.2 proves that this is the case. The 0.5 difference indicate the filter's time constant of the frequency controller.

5.3 Different converter ratings

It was evidenced in the previous study case that for FCR-D, the battery capacity is not the limiting factor, but rather the rating of the converter. So it was decided to increase the rating of the converter from 50 MW to 100 MW and 150 MW to see how this would impact the compensating capability and the SOC.

Figure 5.4 shows the frequency measurements after a 300 MW loss of generation. For this case, generator G1013 was tripped.

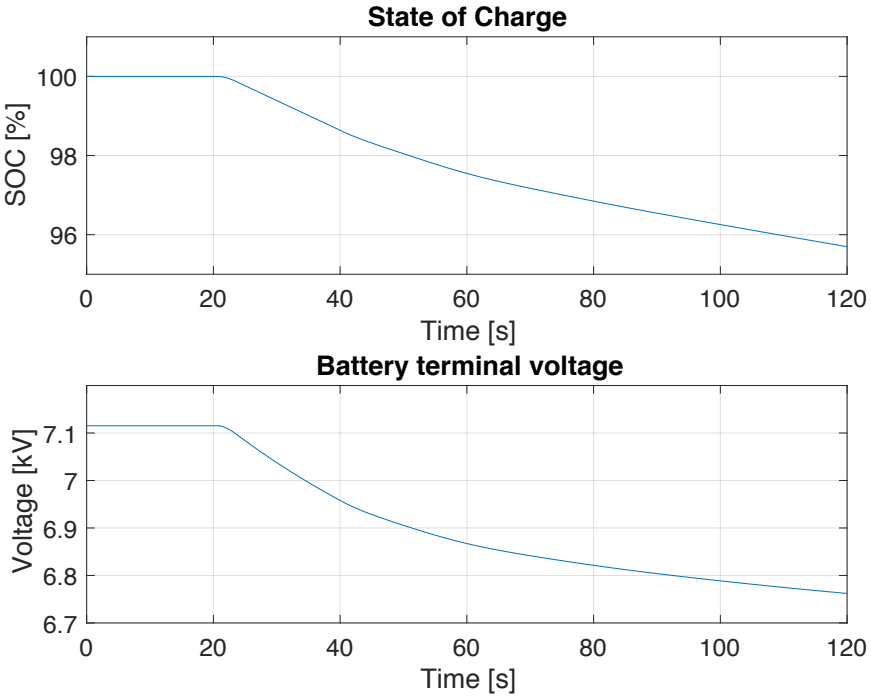

Figure 5.3: Battery states of a a 50 MW, 300 MWh BESS after the loss of 750 MW of generation

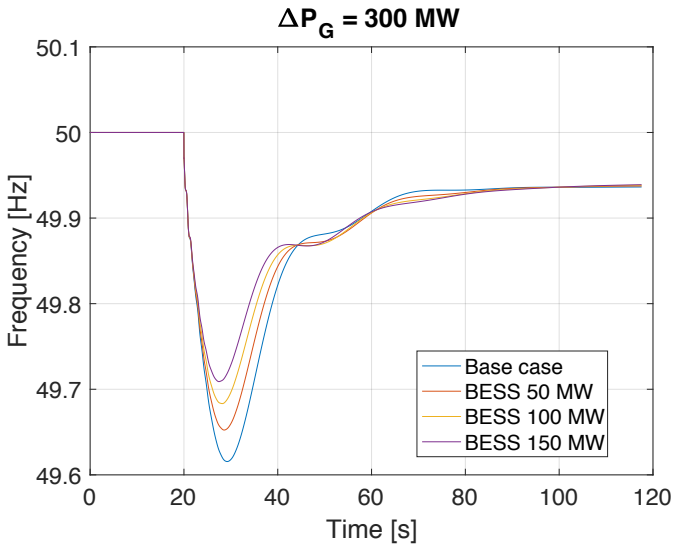

Figure 5.4: Frequency measurements comparing the effect of converter rating for the same frequency event caused by the loss of 300 MW of generation

Looking at Figure 5.4, it is clear that the higher the rating of the converter, the more the BESS is able to reduce the Nadir. Figure 5.5 shows the active power measurements and SOC levels for the same event frequency event but for converter ratings of 50 MW, 100 MW and 150 MW.

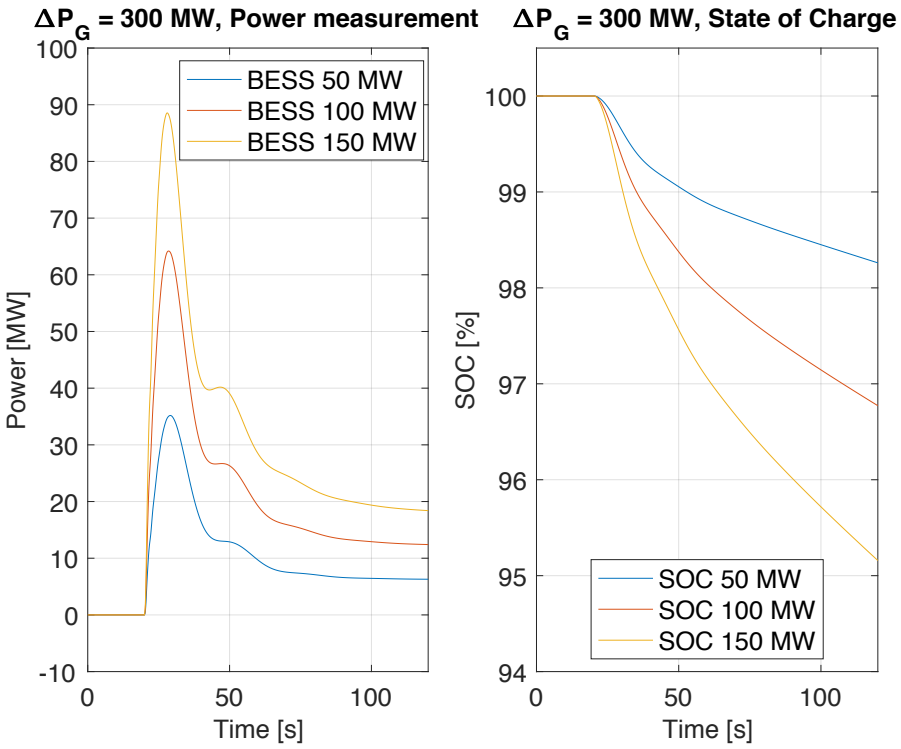

Figure 5.5: Power and SOC measurements comparing the effect of converter rating for the same frequency event caused by the loss of 300 MW of generation

5.4 Decommissioning of thermal plants in the Southwest zone

One of the challenges that the power system faces is the reduction of system inertia caused by the replacement of conventional generation with energy sources that are decoupled from the grid, such as wind power. Currently, Sweden is in a nuclear phase-out process: the decommissioning process of the reactor Oskarshamn 2 has already begun at the time of this writing, while the phase-out of Oskarshamn 1 is planned to begin by the end of 2017. On the other hand, Oskarshamn 3, rated 1450 MW, is one of the world's largest boiling water reactors and it is expected to remain in operation until the end of its life cycle. Together, they make up 2603 MW of installed capacity, with an approximate daily output of 1600 MW at the time of this writing [31].

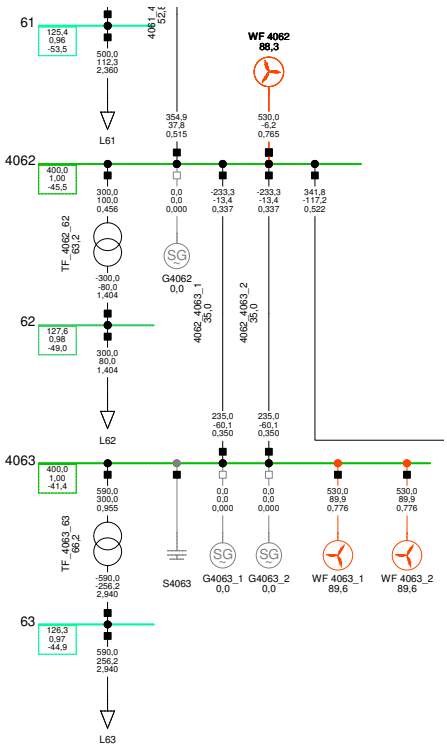

Figure 5.6: Decommissioning of generators G4062, G4063_1 and G4063_2 for wind farms with the same power output in the Southwest zone

However, it can be argued that all nuclear power in Sweden will be replaced by other forms of generation in the future. Having those facts in mind, it was decided to set up a study case simulating the scenario of a complete decommissioning of O1,O2 and O3 in the Nordic32 bus system. For that purpose, conventional generation representing nuclear power plants with an approximate power output to the reactors at Oskarshamn, were replaced by wind power in the Southwest zone without any of the conventional actions taken to compensate the system's weakening. The newly commissioned wind farms are illustrated in Figure 5.7. The decommissioning of

generators G4062, G4063_1 and G4063_2, adding up to 1800 MW, for wind farms with the same power output, is equivalent to the loss of 10,800 MWs (16.7% of the total system inertia).

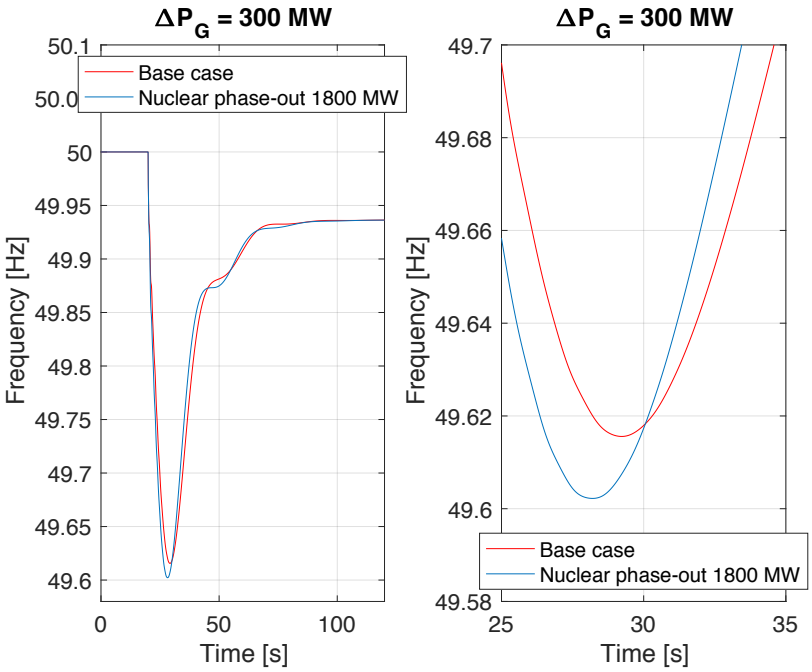

Figure 5.7: Frequency measurements after the loss of 300 MW of generation. The blue line represents the case were a part of the thermal generation has been replaced by wind power. The right plot is a zoom of the frequency Nadir

Figure 5.7 depicts the frequency measurements after the loss of 300 MW of generation at 20 s. The red curve is the base case and the blue curve represents the case where nuclear power has been replaced by wind in the Southwest zone. The picture shows that the system is less robust since the same frequency event results in a larger RoCoF and a lower Nadir.

The base case of loss of 300 MW with BESS compensation is presented in n Figure 5.8, where the BESS reduced the Nadir by 36.333 mHz. The same frequency event on the weaker grid is shown in Figure 5.9, where the action of the proposed ancillary service reduced the Nadir by 39.54 mHz. This is equal to an increased compensating effectiveness of 8.11% when the BESS is supporting weaker grids.

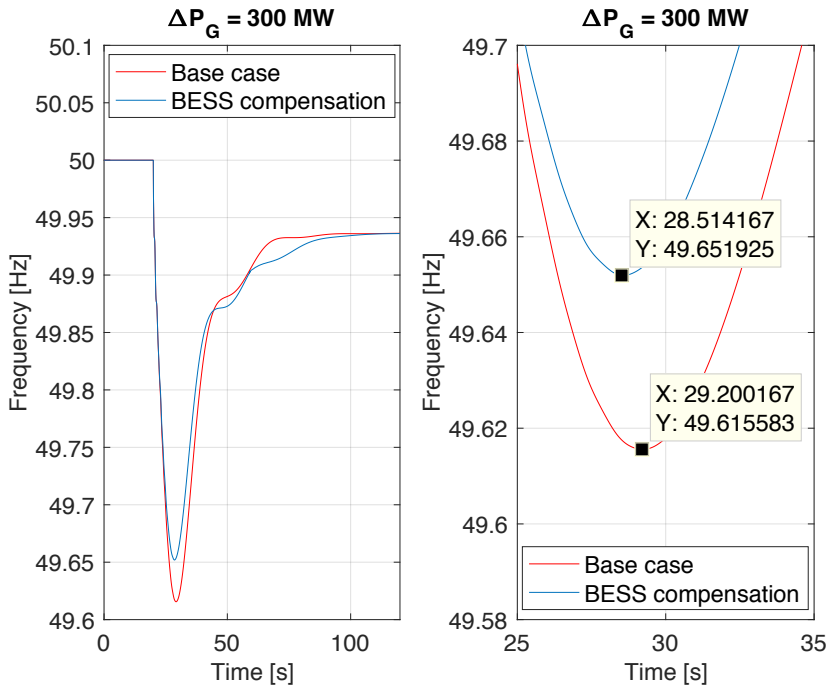

Figure 5.8: Frequency measurements for a 300 MW loss of generation. The right plot is a zoom of the frequency Nadir. 50 MW, 300 MWh BESS

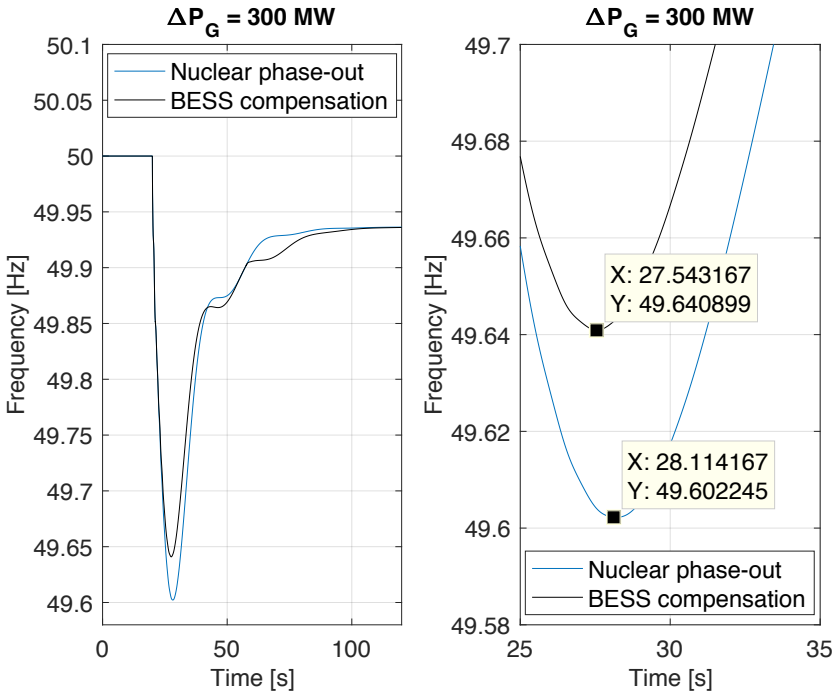

Figure 5.9: Frequency measurements for a 300 MW loss of generation in the case where nuclear has been replaced by wind power. The right plot is a zoom of the frequency Nadir. 50 MW, 300 MWh BESS

6

Discussion

6.1 Sustainable development

Not all issues related to the content of this report are of technical nature. Other important aspects such as sustainable development also play an important role. It results interesting to discuss the possible ramifications that the proposed ancillary service may have from sustainable development point of view.

One could argue that the implementation of BESS providing frequency support, could bolster the adoption of RES into the grid. RES are intermittent in nature: the sun doesn't' always shine and the sometimes there is no wind. This introduces not only uncertainties in the supply that could inflate the energy prices, but also the possibility to have larger frequency deviations due to more frequent imbalances in generation and load. Dedicated BESS to provide frequency support, could allow RES to permeate more in the power system without compromising its robustness or efficiency.

Additionally, BESS are one of the most flexible energy storage systems, with many possible applications like voltage support, energy arbitrage, synthetic inertia, etc. An increased number of BESS would create new market opportunities to provide AS. Aggregators are a good example: specialized companies with a large portfolio of BESS owners could manage their costumers BESS in order to maximize their units availability and profitability, consequently providing more incentives to further develop the technology and to make investments in the sector.

6.2 Areas of opportunity

In order to fully evaluate the value of a BESS as ancillary service, it is worth exploring the areas of opportunity presented in the following (non-exclusive) list:

- Perform a study to find out the optimal rating and capacity of a BESS intended for FCR-D.
- Compare the impact on the system, efficiency and ratings of utilities providing synthetic inertia versus dedicated BESS providing primary frequency control.
- Design and implement a battery State of Health function to the BMS.

- Expand the model to include the losses incurred in the energy conversion stages and estimate the efficiency of the system.
- Carry out the discretization of the controller.
- Design an optimal PWM switching strategy for the system.
- Conduct simulations with several small independent BESS distributed over the network and study their response in the event of a frequency event.
- Investigate the BESS impact on the small-signal stability of the system.
- Look into the effect of a BESS in voltage stability.
- Conduct long-time analysis of the system with real frequency measurements to estimate the life cycle of the BESS.
- Carry out an economic feasibility study of a BESS when used to procure frequency support only.
- Study the differences in size, price, efficiency when using different battery technologies.
- Implement an energy-arbitrage function alongside the frequency-support service to maximize the availability and profitability of the BESS and compare with the case of pure frequency-support.
- Explore the development of an aggregator model that clusters several small-scale BESS and analyze optimal charge/discharge algorithms.

7
Conclusions

A model of a battery-based ancillary service to provide frequency support in the Nordic power system was developed and implemented in PowerFactory. It consists of a battery storage device, a battery management system, a voltage source converter and a phase reactor at the point of connection to the grid. The proposed ancillary service was tested with dynamic simulations in the Nordic32A bus system with the load flow setting LF32_028.

Three study cases were conducted as part of the application study. In the first case, a large generating unit was tripped, resulting in the frequency dropping below 49 Hz. Then, the same frequency event was applied when the system was equipped with the proposed ancillary service. The results proved that the battery was able to provide enough supporting power to prevent the frequency from going below 49 Hz, implying that its compensating action could have avoided the trigger of more drastic frequency-control actions like load-shedding.

On the second study case, the effect of converter ratting was studied compared to battery capacity when the system was used to provide FCR-D. It was concluded that for single, short frequency events, the limiting factor in the proposed ancillary service was the rating of the converter and not the capacity of the battery.

The last study case was the hypothetical scenario of a large phase-out of thermal plants and their replacement with wind power without any of the conventional actions taken to compensate the system's weakening. It was demonstrated that the proposed ancillary service is more effective when compensating weaker grids, since the action of the battery was able to decrease the Nadir by an additional 8.11% in the grid where conventional generation was replaced by static generation for the same frequency event.

Bibliography

[1] ENTSO-E, "Nordic balancing philosophy." http://www.svk.se/contentassets/bc60c82ceaec44c0b9ffbf3ee2126adf/nordic-balancing-philosophy-160616-final_external.pdf, 2016. Online accessed February 2017.

[2] E. Commission, "Vision and strategy for europe's electricity networks of the future." http://www.smartgrids.eu/documents/vision.pdf, 2006. Online accessed January 2017.

[3] E. Commission, "Strategic deployment document for europe's electricity networks of the future." http://www.smartgrids.eu/documents/SmartGrids_SDD_FINAL_APRIL2010.pdf, 2008. Online accessed January 2017.

[4] B. M. Buchholz and Z. Styczynski, *Smart Grids - Fundamentals and Technologies in Electricity Networks*. Springer Berlin Heidelberg, 2014.

[5] H. Holttinen *et al.*, "Ancillary services: technical specifications, system needs and costs." http://orbit.dtu.dk/files/72251308/Ancillary_Services.pdf, 2012. Online accessed January 2017.

[6] Nordel, "Nordic grid code 2007." https://www.entsoe.eu/fileadmin/user_upload/_library/publications/nordic/planning/070115_entsoe_nordic_NordicGridCode.pdf, 2007. Technical Report, Nordel.

[7] K. Walve, "Nordic32a - a cigre test system for simulation of transient stability and long term dynamics," 1993. Svenska Kraftnät, Rev-1994-03-01.

[8] P. Kundur, *Power System Stability and Control*. MacGraw-Hill Incorporated, 1994.

[9] EURELECTRIC, "Ancillary services- unbundling electricity products – an emerging market." http://www.eurelectric.org/Download/Download.aspx?DocumentID=13934, 2004. Online accessed January 2017.

[10] E. Commission, "The system operation guideline." https://ec.europa.eu/energy/sites/ener/files/documents/SystemOperationGuideline%20final%28provisional%2904052016.pdf, 2004. Draft 2016. Online accessed January 2017.

[11] M. Bohlen and F. Hassan, *Integration of Distributed Generation in the Power System*. John Wiley & Sons Incorporated, 2011.

[12] ENTSO-E, "Nordic system operation agreement appendices, english translation." https://www.entsoe.eu/Documents/Publications/SOC/Nordic/System_Operation_Agreement_appendices%28English_2016_update%29.pdf, 2016. Online accessed February 2017.

[13] EPRI, "Electricity energy storage technology options – a white paper primer on applications, costs, and benefits." http://files.energystorageforum.com/Epri_White_Paper.pdf, 2010. Online accessed February 2017.

[14] R. Baxter, *Energy storage: a nontechnical guide*. PennWell, 2007.

[15] M. T. Lawder *et al.*, "Battery energy storage system (bess) and battery management system (bms) for grid-scale applications," *Proceedings of the IEEE*, vol. 102, pp. 1014 – 1030, June 2014.

[16] J. Warner, *The handbook of lithium-ion battery pack design: chemistry, components, types and terminology*. Elsevier Incorporated, 2015.

[17] H. J. Bergveld *et al.*, *Battery Management Systems: Design by Modelling*. Springer Netherlands, 2002.

[18] N. Mohan *et al.*, *Power Electronics; Converters, Applications and Design*. Wiley, 2003.

[19] O. Lennerhag and V. Träff, "Modelling of vsc-hvdc for slow dynamic studies." http://publications.lib.chalmers.se/records/fulltext/183930/183930.pdf, 2013. Master's Thesis, Chalmers University of Technology, Gothenburg, Sweden.

[20] M. Karimi-Ghartemani, *Enhanced Phase-Locked Loop Structures for Power and Energy Applications*. IEEE/Wiley, 2014.

[21] L. Harnefors, "Control of variable speed drives," 2002. Compendium. Department of Electronics, Mälardalen University, Västerås, Sweden.

[22] M. Dürr *et al.*, "Dynamic model of a lead acid battery for use in a domestic fuel cell system," *Journal of Power Sources*, vol. 161, no. 2, pp. 1400 – 1411, 2006.

[23] O. Tremblay *et al.*, "A generic battery model for the dynamic simulation of hybrid electric vehicles," *2007 IEEE Vehicle Power and Propulsion Conference*, pp. 284 – 289, 2007.

[24] O. Tremblay and L. Dessaint, "Experimental validation of a battery dynamic model for ev applications," *World Electric Vehicle Journal*, pp. 289 – 298, 2009.

[25] I. Serban and C. Marinescu, "Control strategy of three-phase battery energy storage systems for frequency support in microgrids and with uninterrupted supply of local loads," *IEEE Transactions on power electronics*, vol. 29, no. 19, pp. 5010 – 5020, 2014.

[26] DIgSILENT, "Powerfactory version 2016 user manual," 2016. Online edition.

[27] DIgSILENT, "Powerfactory technical reference documentation," 2016. Static Generator ElmGenstat.

[28] G. Pinares *et al.*, "On the analysis of the dc dynamics of multi-terminal vsc-hvdc systems using small signal modeling," *2013 IEEE Grenoble Conference PowerTech*, 2013.

[29] D. O. Energy, "United states department of energy global energy storage database." http://www.energystorageexchange.org/projects, 2017. Online accessed June 2017.

[30] E. C. Mitsubishi, "Mitsubishi electric delivers high-capacity energy-storage system to kyushu electric power's buzen substation." http://www.mitsubishielectric.com/news/2016/pdf/0303-b.pdf, 2016. Online accessed June 2017.

[31] O. Aktiebolag, “Om okg.” http://www.okg.se/sv/Om-OKG/, 2016. Online accessed June 2017.

A

Per-Unit values

In the fields of electrical power engineering, electrical machines and drives, it is common to use normalized or *per-unit* values. This normalization has several benefits. For one, most normalized values tend to lie within the range of 0 and 1 $p.u.$. This is quite convenient for calculations in power systems and drives, specially compared to standard values, where the range of order of the units involved in a single calculation can vary from micro to kilo. Another notable benefit when using $p.u$ in power system calculations is that the factor $\sqrt{3}$ for three-phase systems and the winding ratio of the transformers need not be used. Also, to have variables confined within a range of 0 to 1 facilitates the use of control algorithms that are to be digitally implemented [21].

The steps to normalize the unit system can be condensed as follows:

- Pick an apparent power base, S_{base}, for the whole system.
- Choose a base voltage for a bus. The V_{base} at all the other buses are decided by their rating and the transformer ratio, if any.
- Find the base impedance Z_{base} for the different sections of the system and convert all impedances to consistent per-unit terms.

To summarize, a recollection of important per-unit conversions, where the subscript $_n$ indicates normalized quantities:

$$\text{Voltage} \quad : \quad V_{base} \Rightarrow v_n = v/V_{base} \tag{A.1}$$

$$\text{Impedance} \quad : \quad Z_{base} \Rightarrow z_n = V_{base}^2/S_{base} \tag{A.2}$$

$$\text{Angular frequency} \quad : \quad \omega_{base} \Rightarrow \omega_n = \omega/\omega_{base} \tag{A.3}$$

This allows the normalization of resistances and inductances as follows:

$$R_n = \frac{R}{Z_{base}},\ L_n = \frac{\omega_{base} L}{Z_{base}} = \frac{X_L}{Z_{base}} \tag{A.4}$$

where X_L is the inductive reactance at base frequency.

B

Transformations for three-phase systems

B.1 Transformation of three-phase quantities into vectors

A three-phase positive system constituted by the three quantities $v_a(t), v_b(t)$ and $v_c(t)$ can be transformed into a vector in a complex reference frame, usually called $\alpha\beta$ frame, by applying the transformation defined by

$$\underline{v}(t) = v_\alpha + jv_\beta = K\Big(v_a(t) + v_b e^{j\frac{2}{3}\pi}(t) + v_c e^{j\frac{3}{2}\pi}(t)\Big) \tag{B.1}$$

where the factor K is equal to $\sqrt{3/2}$ or $3/2$ to ensure power invariance or voltage invariance, respectively, between the two systems. Equation (B.1) can be expressed as a matrix equation as follows:

$$\begin{bmatrix} v_\alpha \\ v_\beta \end{bmatrix} = K \cdot C_{23} \begin{bmatrix} v_a(t) \\ v_b(t) \\ v_c(t) \end{bmatrix} \tag{B.2}$$

where C_{23} is defined as

$$\begin{bmatrix} \frac{2}{3} & -\frac{1}{3} & -\frac{1}{3} \\ 0 & \frac{1}{\sqrt{3}} & -\frac{1}{\sqrt{3}} \end{bmatrix} \tag{B.3}$$

Similarly, the inverse transformation is calculated as

$$\begin{bmatrix} v_a(t) \\ v_b(t) \\ v_c(t) \end{bmatrix} = K \cdot C_{32} \begin{bmatrix} v_\alpha \\ v_\beta \end{bmatrix} \tag{B.4}$$

where C_{32} represents the rotation matrix

$$\begin{bmatrix} 1 & 0 \\ -\frac{1}{2} & \frac{\sqrt{3}}{2} \\ -\frac{1}{2} & -\frac{\sqrt{3}}{2} \end{bmatrix} \tag{B.5}$$

B.2 Transformation between fixed and rotating coordinate systems

Let the vectors $\underline{v}$(t) and $\underline{u}$(t) rotate in the $\alpha\beta$ frame with the angular frequency $\omega(t)$ in the positive sequence (counter-clockwise) as illustrated on Figure B.1. The angle $\theta(t)$ is the phase angle between the vector $\underline{u}$(t) and the α axis.

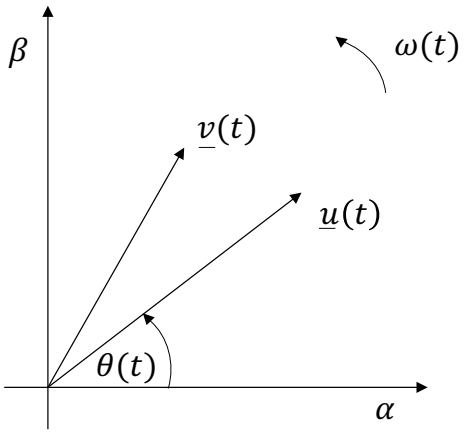

Figure B.1: Two sample vectors, $\underline{v}$(t) and $\underline{u}$(t), rotating in the positive sequence with constant frequency in the fixed reference frame $\alpha\beta$

If the vector $\underline{u}$(t) is taken as the d axis of a dq frame that rotates in the same direction with the same angular frequency $\omega(t)$, both vectors will appear as fixed vectors in that frame. The components of $\underline{v}$(t) in the dq frame are thus given by the projections of the vector on the direction of $\underline{u}$(t) and on the orthogonal direction, as illustrated in Figure B.2.

The transformation can be written in vector form as

$$\underline{v}^{dq}(t) = \underline{v}^{\alpha\beta}(t)e^{-j\theta(t)} \tag{B.6}$$

with the angle $\theta(t)$, as depicted in Figure B.2 by

$$\theta(t) = \theta_0 + \int_0^{\tau} \omega(\tau)\,\mathrm{d}\tau \tag{B.7}$$

Similarly, the inverse transformation, from the rotating dq frame to the fixed $\alpha\beta$ frame is defined by

$$\underline{v}^{\alpha\beta}(t) = \underline{v}^{dq}(t)e^{j\theta(t)} \tag{B.8}$$

The components in the dq frame can be determined from Figure B.2, which in matrix form is given by

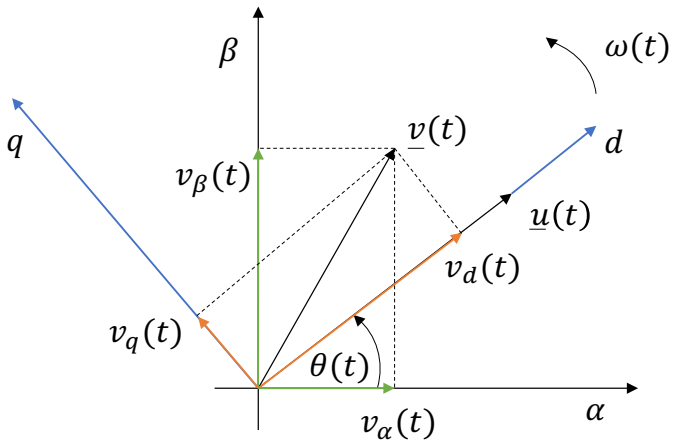

Figure B.2: Relation between the stationary $\alpha\beta$ reference frame and the rotating dq reference frame. Vector $\underline{u}$(t) is taken as reference for the d axis

$$\begin{bmatrix} v_d(t) \\ v_q(t) \end{bmatrix} = R\big(-\theta(t)\big) \begin{bmatrix} v_\alpha(t) \\ v_\beta(t) \end{bmatrix} \tag{B.9}$$

while the inverse is given by

$$\begin{bmatrix} v_\alpha(t) \\ v_\beta(t) \end{bmatrix} = R\big(\theta(t)\big) \begin{bmatrix} v_d(t) \\ v_q(t) \end{bmatrix} \tag{B.10}$$

where the projection matrix $R\big(\theta(t)\big)$ is

$$\begin{bmatrix} cos(\theta(t)\big) & -sin(\theta(t)\big) \\ sin(\theta(t)\big) & cos(\theta(t)\big) \end{bmatrix} \tag{B.11}$$

C

Nordic32A

C.1 PowerFactory implementation

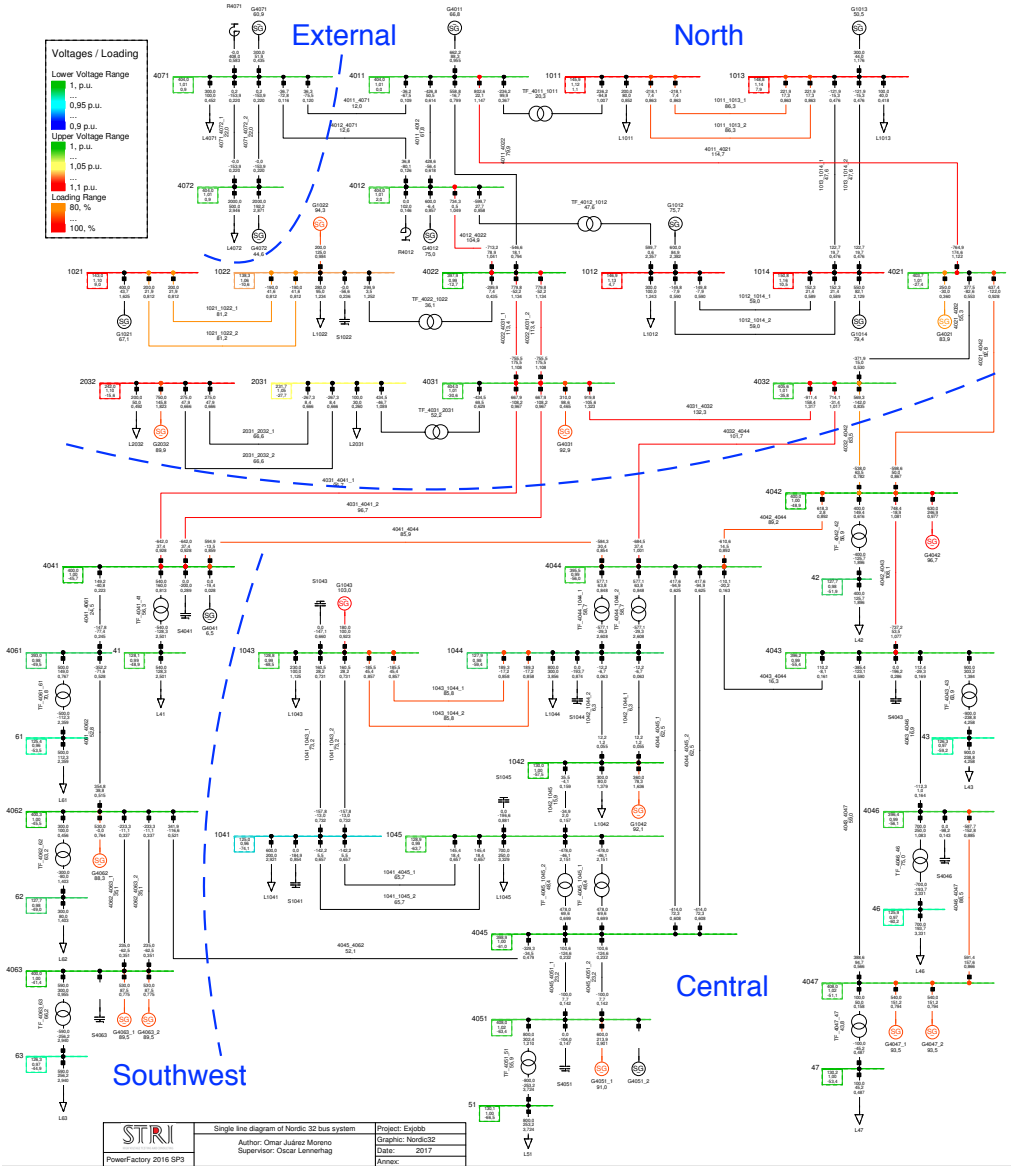

Figure C.1: PowerFactory single-line diagram of the Nordic 32 bus system showing the results of the load flow LF23_28 with high transfers

C.2 Load flow LF32_028 results

		DIgSILENT PowerFactory 2016 SP3	Project:
			Date: 6/5/2017

Load Flow Calculation			Grid Summary
AC Load Flow, balanced, positive sequence		Automatic Model Adaptation for Convergence	No
Automatic Tap Adjust of Transformers	Yes	Max. Acceptable Load Flow Error for	
Consider Reactive Power Limits	Yes	Nodes	1,00 kVA
		Model Equations	0,10 %

Grid: Nordic32	System Stage: Nordic32	Study Case: BC	Annex: / 1

Grid: Nordic32 Summary

No. of Substations	32	No. of Busbars	42	No. of Terminals	555	No. of Lines	52
No. of 2-w Trfs.	18	No. of 3-w Trfs.	0	No. of syn. Machines	22	No. of asyn.Machines	0
No. of Loads	22	No. of Shunts	11	No. of SVS	0		

Generation	=	11362,23	MW	2017,10	Mvar	11539,89	MVA
External Infeed	=	0,00	MW	0,00	Mvar	0,00	MVA
Inter Grid Flow	=	0,00	MW	0,00	Mvar		
Load P(U)	=	10940,00	MW	3358,43	Mvar	11443,89	MVA
Load P(Un)	=	10940,00	MW	3358,43	Mvar	11443,89	MVA
Load P(Un-U)	=	0,00	MW	0,00	Mvar		
Motor Load	=	0,00	MW	0,00	Mvar	0,00	MVA
Grid Losses	=	422,23	MW	-473,99	Mvar		
Line Charging	=			-4364,98	Mvar		
Compensation ind.	=			510,05	Mvar		
Compensation cap.	=			-1377,39	Mvar		
Installed Capacity	=	16700,00	MW				
Spinning Reserve	=	5187,77	MW				

Total Power Factor:			
Generation	=	0,98	[-]
Load/Motor	=	0,96 / 0,00	[-]

Figure C.2: PowerFactory output displaying the results of the load flow LF23_28 with high transfers